

Effect of shrinkage induced flow on solutal instability and macro-segregation during directional solidification of binary alloys

5.1 INTRODUCTION

During the solidification process of both metallic and non-metallic alloys, the melt undergoing the process manifests three distinct regions containing three different phases. These three distinct regions consist of pure solid, pure liquid, and mushy phase characterised by the coexistence of both solid and liquid phases. Unidirectional solidification in the bottom-up direction promotes two entirely different variations of mushy zone formation depending upon the solute-solvent constituent of the alloy system. Since the solubility of the solid phase is always less than that of the liquid phase. Liquid to solid phase transformation causes solute rejection in the melt adjacent to the newly transformed solid region. As a result, the melt adjacent to the solid regions gets enriched in solute content, and a strong solute concentration is established in the melt adjacent to the solid phase. If the solute is heavier than the solvent, then the solute rich melt adjacent to the solid phase gets heavier. In the case of bottom-up solidification orientation, the melt is stably stratified when it comes to the thermal buoyancy effect. The heavier solute rejection to the melt due to solid formation at the bottom during bottom-up solidification reinforces this stability of the buoyancy field, leading to a rich solute concentration near the bottom surface, known as inverse segregation. For alloy systems with heavier solute and lighter solvent, the mushy region manifests a planer front growth with inverse segregation. On the other hand, if the solute is lighter than the solvent, then the rejected excess solute in the melt adjacent to the solid region causes instability in the solutal buoyancy field. If this instability in the solutal buoyancy field is strong enough to overcome the stability of the thermal buoyancy field, the convection in the form of a plume ensues. As a result, the mushy region is typically characterised by interspersed channels formations at the plume locations. Therefore, melt flow during solidification of alloys defined by the solutal buoyancy field has a profound effect on the growth of the mushy region and hence the overall macro-segregation. The presence of shrinkage induced flow and its interaction with the solutal convection augments the challenges associated with modeling of mushy front growth and overall macro-segregation further. In essence, a realistic prediction of overall macro-segregation for the bottom-up alloy solidification process must account for the interaction between shrinkage induced, and solutal convection within the solidification domain [Flemings, 1974; Fisher, 1981]. Since the bottom-up solidification process is of primary interest to many industrial applications involving single crystal growth, understanding the combined effect of shrinkage induced and solutal convection on overall macro-segregation is of utmost importance.

In a bottom cooled cavity, the growth of a solid front occurs along a vertically upward direction. The thermal gradient along the vertically upward direction is positive with a stably stratified thermal buoyancy field. The thermal expansion coefficient is positive without any ambiguity, indicating the expansion of overall volume with increasing temperature and vice versa. However, depending on the relative heaviness or lightness of the solute with respect to the solvent, the solutal expansion coefficient needs to be assigned with negative or positive values. If the rejected solute to the melt during the alloy solidification process is heavier than the solvent, the

solubility expansion coefficient is negative, indicating overall volume reduction of solute enriched melt. For bottom-up solidification orientation, the negative solubility expansion coefficient leads to stable stratification of the solubility buoyancy field, reinforcing a stably stratified thermal buoyancy field. On the other hand, the rejection of lighter solute in the melt during the alloy solidification process assigns a positive solubility expansion coefficient, indicating an overall volume expansion of the solute enriched melt. For directional alloy solidification with bottom cooling orientation, volume expansion of solute enriched melt adjacent to the growing solid front from the bottom promotes instability of the solubility buoyancy field that might lead to the formation of plumes.

The formation of the mushy region extending between the pure solid and pure liquid region can also be explained by the solute rejection phenomena during the liquid to solid phase transformation process [Flemings, 1974; Worster, 1986, 1991, 1992; Worster and Kerr, 1994; Stefanescu, 2015; Dantzig and Rappaz, 2016; Zhang et al., 2020; Xie et al., 2020]. Since the melt adjacent to the newly transformed solid-phase gets enriched with solute concentration, a depression of liquidus temperature occurs for the solute rich melt. This depression of liquidus temperature causes a delay in the further solidification process of the liquid-rich melt. Meanwhile, the regions beyond the solute rich melt with leaner solute concentration and higher liquidus temperature cools down sufficiently to attain this comparatively higher liquidus temperature. As a result, liquid to solid phase transition ensues beyond the region with solute rich melt causing farther solute rejection and farther spreading of a region with solid-phase dispersed within a solute rich melt. However, the region adjacent to the cold boundary being the coldest region, complete solidification is eventually attained in this region with the local temperature approaching the eutectic temperature of the alloy system. Thus, we obtain a solidification domain characterized by a pure solid and liquid region separated by a region of dispersed solid phase within a solute rich melt known as a mushy region. Since the solubility gradient in the melt is predominant within the mushy region, the instability of the solubility buoyancy field primarily ensues from the mushy region itself. Depending on the strength of this instability, the effect can be farther propagated to the pure liquid region. The aiding or opposing nature of the interaction between the thermal and solubility buoyancy fields regulates the melt convection within and beyond the mushy region, defining its growth [Sarazin and Hellawell, 1988; Felicelli et al., 1991; Jamgotchian et al., 2004]. Since macro-segregation in the final cast product is of direct consequence of the mushy zone growth mechanism, it is extremely important to study the effect of solubility instability on the evolution of the mushy region.

Inverse segregation encountered due to the heavier solute rejection in the melt during solidification of the binary alloy has been studied and explained by several researchers [Diao and Tsai, 1993; Chen and Tsai, 1993; Gao et al., 2017, 2019]. Similarly, channel formation in the mushy region due to lighter solute rejection in the melt during the directional solidification of metal alloys [Sarazin and Hellawell, 1988; Felicelli et al., 1991; Bergman et al., 1997] or inorganic alloys [Chen and Chen, 1991; Emms and Fowler, 1994; Chen et al., 1994; Chen, 1995; Kumar et al., 2019] is a well-studied subject area for many decades. Simulations considering shrinkage induced flow performed by Diao and Tsai [1993]; Chen and Tsai [1993] successfully predicted the inverse segregation during the bottom-up solidification of Al-Cu alloy. However, the model binary system considered [Diao and Tsai, 1993; Chen and Tsai, 1993], is not conducive to promote freckle formation due to heavier solute rejection in the melt during the liquid-solid phase transition. Chiarelli et al. [1994]; Chiarelli and Worster [1995] considered the effect of a density difference between fluid and solid in the absence of solubility buoyancy effect and analysed the mushy layer instability with the conclusion that the instability can occur only in the case of expansion. Numerical models proposed by Schulze and Worster [1998]; Chung and Worster [2002] were distinctly focused on obtaining steady-state solutions for the problems with specified channel positions. However, these models do not address the cause and onset of channel formation; neither do they analysed the flow interaction between the adjacent channels. Katz and Worster

[2008] proposed a 2-D numerical model based on Darcy's law and the enthalpy method to avert imposing explicit conditions on the solid-mushy-liquid interfaces. The analysis was performed using $\text{NH}_4\text{Cl-H}_2\text{O}$ solution, and the results obtained were compared with the experimental data presented by Peppin et al. [2008]. Further, Chakraborty and Dutta [2013] numerically modeled the freckle formation during bottom-up solidification of $\text{NH}_4\text{Cl-H}_2\text{O}$ solution. The detachment and advection of solid particles along with the melt were observed experimentally and implemented numerically. However, the shrinkage effect was unaccounted for during the solidification process. Recently, an experimental investigation was carried out by Kumar et al. [2018a] to address the effect of solutal composition over freckle formation for $\text{NH}_4\text{Cl-H}_2\text{O}$ binary solution. The study was further extended to investigate the role of mushy zone permeability in driving the buoyancy flow patterns in faceted and dendritic growth during bottom-up solidification of $\text{KNO}_3\text{-H}_2\text{O}$ and $\text{NH}_4\text{Cl-H}_2\text{O}$ binary solution, respectively [Kumar et al., 2020]. The results showed a peculiar behaviour of decreasing and sudden increase in temperature during solidification for KNO_3 aqueous solution as compared to a monotonous decrease in temperature for $\text{NH}_4\text{Cl-H}_2\text{O}$ solution. In addition to double-diffusive convection during directional solidification, Anderson and Worster [1996]; Guba and Worster [2010]; Roy et al. [2020] studied an oscillatory instability within the mushy region, which was later modified for ternary alloy system by Guba and Anderson [2014].

Although the effect of shrinkage induced flow has been considered for the micro-scale solidification [Narski and Picasso, 2007; Bhattacharya and Dutta, 2014; Bhattacharya, 2019] and at macro-scale to model inverse segregation associated with heavier solute rejection during bottom-up solidification of Aluminium-4.1 wt.% Copper alloy [Diao and Tsai, 1993; Chen and Tsai, 1993], studies involving the effect of shrinkage induced flow on freckle formation is rarely found [Sajja and Felicelli, 2011]. Challenges associated with the modeling of freckling phenomena during directional solidification of the binary alloy due to rejection of lighter solute in the melt become much more formidable when additional complexities involving the inclusion of shrinkage induced flow is accounted. Therefore, modeling channel formation in the mushy region and associated macro-segregation arising from the coupled interaction between shrinkage induced and solutal convection poses a very interesting endeavour. Since no such study has been reported so far, the present work focuses on developing a numerical model to study the effect of shrinkage induced flow on freckle formation during bottom-up directional solidification of metal alloys. The solid-mushy and mushy-liquid interface is captured by employing the novel volume fraction updating method based on the fixed grid method. Before conducting the study involving the effect of shrinkage induced flow on channel formation, the model is validated with the existing results concerning inverse segregation investigation associated with heavier solute rejection in the melt during bottom-up solidification of Aluminium-4.1 wt.% Copper binary alloy [Diao and Tsai, 1993; Chen and Tsai, 1993; Kato and Cahoon, 1985]. Once the validation of the present model provided reasonable agreement with the existing results, we extended our study to analyse the interactions between the shrinkage induced flow and solutal instability associated with freckle formation during bottom-up solidification of model binary alloy system Aluminium-30 wt.% Magnesium. The study is aimed at obtaining a realistic prediction of freckle formation and corresponding macro-segregation during directional solidification of binary alloys under the influence of shrinkage induced flow.

5.2 MATHEMATICAL MODELING

The numerical model discussed in previous section 4.2 is further extended for the alloy solidification and is based on continuum formulation proposed by Bennon and Incropera [1987a,b]. In addition to the previous assumptions (section 4.2), it is assumed that the phases within the binary zone satisfy the thermodynamic equilibrium, whereas the relative velocity of the solid phase is zero. Following these assumptions, the governing equations for continuity, momentum, energy,

and species corresponding to two-dimensional binary alloy solidification are given as:

Continuity

$$\frac{\partial}{\partial t}(\rho) + \nabla \cdot (\rho \vec{V}) = 0 \quad (5.1)$$

Momentum

$$\frac{\partial}{\partial t}(\rho u) + \nabla \cdot (\rho \vec{V} u) = \nabla \cdot \left(\mu_l \frac{\rho}{\rho_l} \nabla u \right) - \frac{\partial p}{\partial x} - \frac{\mu_l \rho}{K \rho_l} u - \nabla \cdot \left(\rho \frac{g_s \rho_s}{g_l \rho_l} \vec{V} u \right) + \nabla \cdot \left(\mu_l u \nabla \left(\frac{\rho}{\rho_l} \right) \right) \quad (5.2)$$

$$\begin{aligned} \frac{\partial}{\partial t}(\rho v) + \nabla \cdot (\rho \vec{V} v) = \nabla \cdot \left(\mu_l \frac{\rho}{\rho_l} \nabla v \right) - \frac{\partial p}{\partial y} - \frac{\mu_l \rho}{K \rho_l} v - \nabla \cdot \left(\rho \frac{g_s \rho_s}{g_l \rho_l} \vec{V} v \right) + \nabla \cdot \left(\mu_l v \nabla \left(\frac{\rho}{\rho_l} \right) \right) \\ + \rho_{ref}^l g_a [\beta_T (T - T_{ref}) + \beta_C (C_l - C_{ref})] \end{aligned} \quad (5.3)$$

Energy

$$\begin{aligned} \frac{\partial}{\partial t}(\rho T) + \nabla \cdot (\rho \vec{V} T) = \nabla \cdot \left(\frac{k}{c_{ps}} \nabla T \right) - \nabla \cdot \left[\left(\frac{c_{pl}}{c_{ps}} - 1 \right) \rho \vec{V} T \right] - \frac{\partial}{\partial t} \left(\frac{\rho_s g_l h_{sl}}{c_{ps}} \right) \\ - \frac{\partial}{\partial t} \left[g_l \left(\frac{c_{pl}}{c_{ps}} - 1 \right) (\rho_l T - \rho_s T_e) \right] \end{aligned} \quad (5.4)$$

Species

$$\frac{\partial}{\partial t}(\rho C) + \nabla \cdot (\rho \vec{V} C) = \nabla \cdot (g_l \rho_l D_l \nabla C) + \nabla \cdot [g_l \rho_l D_l \nabla (C_l - C)] - \nabla \cdot [\rho \vec{V} (C_l - C)] \quad (5.5)$$

Significance of each term appearing in Eqns. 5.1 to 5.4 are explained in section 4.2. The sixth term appearing on the right-hand side of the v momentum Eqn. 5.3 represents the combined thermo-solutal buoyancy force, with β_C being defined as solutal expansion coefficient. T_e appearing in energy Eqn. 5.4 is defined as the eutectic temperature of binary alloy system.

The species conservation Eqn. 5.5 is represented in terms of mass averaged mixture concentration of the solute C as the scalar variable. Mass averaged solute concentration C is defined as $C = f_s C_s + f_l C_l$, where, C_s and C_l are the local solid and liquid solute concentrations respectively. For the present formulation, solute diffusivity in solid phase (D_s) is considered to be insignificant as compared to that in liquid phase (D_l) i.e. $D_l \gg D_s$. Therefore, D_s is assigned with zero value implying absence of solute diffusion in solid phase. The second source and third source terms appearing on right hand side of Eqn. 5.5 originate from solute rejection in the melt during the ongoing solidification process. The liquid solute concentration C_l appearing in Eqn. 5.5 is obtained from the mass averaged species concentration and is defined as:

$$C_l = \frac{\rho C}{k_p \rho + (1 - k_p) g_l \rho_l} \quad (5.6)$$

where, k_p is partition coefficient defined as the solute concentration ratio in solid and liquid phases $k_p = C_s / C_l$. Partition coefficient k_p is obtained from the equilibrium phase diagram with the assumption of the slopes of solidus and liquidus lines to be constant. Although the estimation of C_l from Eqn. 5.6 looks quite straight forward, we should be careful while using the same for calculating solute concentration in liquid phase. The maximum obtainable solute concentration in the melt is restricted by eutectic concentration, i.e, the condition $C_l \leq C_e$ condition must prevail in the entire solidification domain. Therefore, any value of $C_l > C_e$ obtained from Eqn. 5.6 must immediately be set to a value $C_l = C_e$ to account for this physical constraint.

5.3 NUMERICAL APPROACH AND PHYSICAL DOMAIN

The governing Eqns. 5.1 to 5.5 are in the standard conservative form as described by Patankar [2018]. The standard advection and diffusion terms are discretized using power-law scheme (Patankar [2018]). Numerical scheme to discretize source terms appearing in Eqns. 5.1 to 5.4 are explained in section 4.3. The source term involving diffusion, on the right hand side of species conservation Eqn. 5.5 is discretized by using central difference scheme, whereas the third term on the right hand side of Eqn. 5.5) is discretized by using first-order upwind scheme. The numerical procedure is carried out by calculating the flow field using the SIMPLER algorithm. Once the flow field is obtained, solution of temperature and species field follows. The solution of flow, temperature and species field is then followed by the evaluation of the local liquid volume fraction using a numerical approach. The volume fraction updating scheme allows us to track the distinct interfaces existing between solid, mushy and liquid regions in a fixed grid framework. The procedure is repeated for each time-step until the flow field and scalar quantities T , C , g_l satisfies the convergence criteria of 10^{-5} . Since the magnitude of the velocity components are of the order of $10^{-3} m$, relative error is considered for the convergence criteria while estimating the flow field. For rest of the scalar parameters convergence criterion are based on absolute error. A line by line tri-diagonal matrix algorithm (TDMA) is used to solve the discretized algebraic equations iteratively.

The numerical scheme to update the liquid volume fraction g_l is obtained by following the steps as proposed in section. 4.3:

$$g_{l_p}^{n+1} = g_{l_p}^n + \lambda \frac{[B_p \rho_l g_{l_p}^n + a_p^0] (T_p^n - T_p^{n+1})}{A_p + B_p (\rho_l T_p^{n+1} - \rho_s T_e)} \quad (5.7)$$

Since, solidification in an elementary control volume can only be achieved when the local temperature of the control volume reaches the liquidus temperature T_L corresponding to the local liquid solute concentration C_l , the value of T_p^{n+1} appearing in Eqn. 5.7 is set to $T_p^{n+1} = T_L$. Thus, the final expression for the liquid volume fraction updating scheme corresponding to binary alloy solidification is obtained as follows:

$$g_{l_p}^{n+1} = g_{l_p}^n + \lambda \frac{[B_p \rho_l g_{l_p}^n + a_p^0] (T_p^n - T_L)}{A_p + B_p (\rho_l T_L - \rho_s T_e)} \quad (5.8)$$

The governing equations Eqns. 5.1 to 5.5 are valid for the entire solidification domain consisting of solid, mushy and liquid phases; thus, the necessity to track the shape and scale of each region is redundant, rendering the numerical scheme to be a fixed grid based approach.

Figure 5.1 represents the schematic of the physical domain of interest consisting of a rectangular cavity with an riser opening located at the centre of the top boundary. All the boundaries except the bottom surface are subjected to thermal insulation. The bottom surface is maintained at a temperature $T_c < T_e$ to ensure the directional solidification from bottom. The entire cavity wall is subjected to no-slip boundary condition, while the riser opening at the center

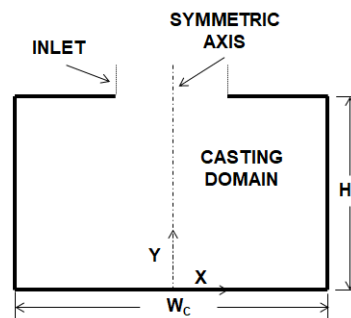


Figure 5.1 : Schematic of the physical domain of interest

Table 5.1 : Binary alloy systems used for numerical analysis and their thermo-physical properties

Properties	Symbol/units	Al-4.1 wt.% Cu	Al-30 wt.% Mg
Thermal conductivity	k (W/mK)	k_l -82.61 / k_s -192.49	k_l -90.7 / k_s -211
Specific heat	c_p (J/kgK)	c_{pl} -1058.8 / c_{ps} -1092.8	c_{pl} -1058.8 / c_{ps} -1092.8
liquid solute Diffusivity	D_l (m^2/s)	3×10^{-9}	3×10^{-9}
Density	ρ (kg/m^3)	ρ_l -2400 / ρ_s -2650	ρ_l -2070 / ρ_s -2190
Latent heat	h_{sl} (J/kg)	397500	398000
Dynamic viscosity	μ (kg/ms)	0.003	0.00138
Thermal expansion coefficient	β_T (K^{-1})	4.95×10^{-5}	2.1×10^{-5}
Solutal expansion coefficient	β_C	-0.0092	0.00428
Partition coefficient	k_p	0.17	0.482
Eutectic temperature	T_e (K)	821.2	723
Melting temperature	T_m (K)	933.2	933.2
Eutectic composition	C_e	33.2	36.3
Initial Temperature	T_i (K)	970	770
Initial composition	C_0	4.1	30

of the top wall is subjected to constant pressure (zero gauge pressure) boundary condition. The numerical simulations are performed for the casting domain of height H_C and width W_C ($H_C \times W_C$). Since the domain of interest is symmetric with respect to the vertical central line, we chose to carry out the computations for one of the symmetric halves to reduce total computational time.

5.4 RESULTS AND DISCUSSION

The bottom-up directional solidification process is instigated once the bottom surface temperature drops down below the liquidus temperature (T_L) of the alloy system (Figure 5.1). The domain undergoing solidification is filled with the molten metal at the initial temperature (T_i) above the liquidus temperature (T_L) of the alloy system. A continuous inflow of molten liquid is assumed to be maintained into the domain through the riser opening at the center of the cavity top surface exposed to atmospheric pressure. Numerical analysis of the bottom-up directional binary alloy solidification process is performed for two different alloy systems, namely: (i) Al-4.1 wt.% Cu alloy, and (ii) Al-30 wt.% Mg alloy. The first case study corresponding to the solidification of Al-4.1 wt.% Cu alloy is carried out to validate the numerical model by comparing model predictions with numerical results reported by Diao and Tsai [1993]; Chen and Tsai [1993]. The second case study corresponding to the solidification of Al-30 wt.% Mg alloy pertains to the investigation of freckle formation under the influence of shrinkage induced flow. The thermophysical properties of Al-Cu alloy [Diao and Tsai, 1993; Chen and Tsai, 1993; Trivedi et al., 2001] and Al-Mg alloy [Geng et al., 2018; Lee et al., 1994; Liu et al., 2017; Mo and Thevik, 1998] used for the present study are enlisted in table. 5.1.

5.4.1 Solidification of Al-4.1 wt.% Cu

The first case study involving bottom-up directional solidification of Al-4.1 wt.% Cu alloy is carried out for validating the proposed numerical model by comparing the model predictions with the numerical[Diao and Tsai, 1993; Chen and Tsai, 1993] and experimental[Kato and Cahoon, 1985] data. The solidification domain consists of a rectangular cavity of dimension 150×20 mm^2 [Diao and Tsai, 1993; Chen and Tsai, 1993]. Solidification is promoted by removing heat continuously from the bottom surface by means of circulation of heat transfer fluid between the bottom surface and a chiller maintained at a temperature of 293 K. The convective heat transfer between the bottom wall and chiller is assigned with an effective heat transfer coefficient of $h_c = 837$ W/ m^2K . All other sides of the domain are assumed to be insulated. The top surface of

the melt is considered to be open, allowing melt flow from above, and subjected to atmospheric pressure [Diao and Tsai, 1993; Chen and Tsai, 1993]. As the melt starts to solidify unidirectionally from the bottom, the positive temperature gradient in the vertically upward direction gives rise to a stably stratified thermal buoyancy field in the melt domain, eradicating the possibility of attaining thermal buoyancy-driven natural convection. For the chosen alloy system, Aluminium and Copper plays the role of solvent and solute, respectively. Due to a much lesser solute (Cu) solubility in the solid phase as compared to the liquid phase, solidification of the Al-4.1 wt.% Cu alloy system leads to rejection of Cu in the melt adjacent to the newly transformed solid phase. Copper, being heavier than Aluminium, Copper enriched melt adjacent to the newly transformed solid phase also becomes heavier, promoting the accumulation of Copper rich melt in the lower region of the cavity. Once again, heavier solute rejection during liquid to solid phase transition leads to a stably stratified solutal buoyancy field eliminating the existence of solutal buoyancy-driven natural convection in the melt. Therefore, the convection field obtained in the cavity is solely associated with the shrinkage induced effects. The predicted solute concentration distribution and temperature distribution from the present model is compared with the existing numerical prediction [Diao and Tsai, 1993; Chen and Tsai, 1993] and is shown in figure 5.2, where the values of scalar variables are the mean average in horizontal direction. Formation of inverse solutal segregation (negative slope of solute concentration inside the solid and mushy region) (figure 5.2(a)) is predicted by both the models, and the agreements between the vertical temperature and solute field predicted by these two models are found out to be reasonable. Marginal difference in the results can be observed within the mushy region concerning solute variation due to slight mismatch between mush-liquid interface location. This slight deviation in interface location also caused a marginal mismatch of temperature profiles in the liquid domain.

Marginal mismatch found during the model validation with existing numerical result compelled us to verify the proposed model against experimental data. Diao and Tsai [1993] and Chen and Tsai [1993] validated their numerical prediction with experimentally obtained solute distribution in the as cast product of Al-4.1 wt.% Cu alloy reported by Kato and Cahoon [1985]. We also compare our model prediction with the experimental results reported by Kato and Cahoon [1985] in a similar manner. This comparison is shown in figure. 5.2(c). Once again reasonable agreement is obtained between the model prediction and experimental data within $\sim 2\%$ error limit.

The reason behind the existence of the negative solutal segregation in the mushy region is worth explaining. From the inception of the solidification process adjacent to the bottom surface, the melt surrounding the newly transformed solid-phase gets enriched with heavier solute (Copper) concentration causing a depression of liquidus temperature of this solute rich melt. The depression of local liquidus temperature hinders the liquid to solid phase transformation of this liquid-rich melt at the bottom of the cavity any farther. However, the regions above the solute rich melt having a leaner solute (Copper) concentration and higher liquidus temperature starts solidifying as the local temperature decreases sufficiently, promoting farther rejection of heavier solute (Copper). The solute rich, heavy melt thus produced in the mushy region keeps leaching in the downward direction, making the cavity bottom filled with liquid melt with ever-increasing solute concentration delaying the solidification process in that region farther. However, the region adjacent to the cold bottom surface being the coldest region in the cavity, complete solidification is eventually attained as the local temperature approaches the eutectic point. The combined effect of the heavier melt leaching in the mushy region and the shrinkage induced flow allows the solute lean melt from the pure liquid region above to percolate inside the mushy region. The mushy region already contains a dispersed solid fraction within it, and the solute content of this dispersed solid phase is much below the nominal solute (Copper) concentration (C_0) of the melt. The entry of solute (Copper) lean melt from the pure liquid region from above causes an overall depression of solute (Copper) concentration (given by $C = f_s C_s + f_l C_l$) below C_0 for a portion of the mushy

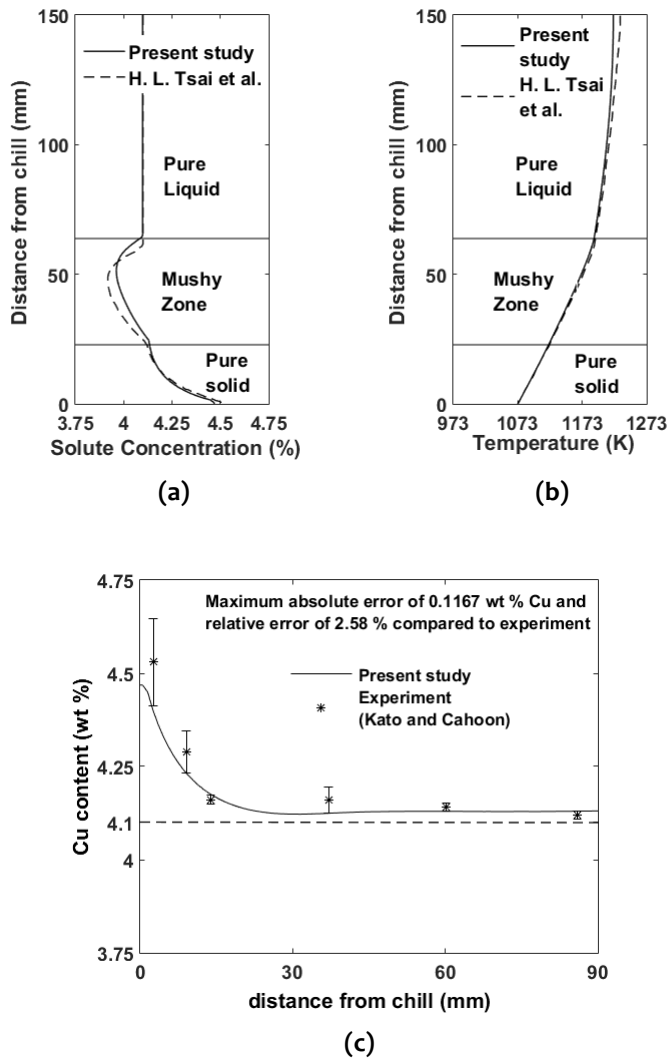


Figure 5.2 : Comparison of (a) solute distribution, and (b) temperature distribution profiles along vertical direction at $t = 180$ s obtained from the present model and the existing numerical model [Diao and Tsai, 1993; Chen and Tsai, 1993], and (c) comparison of final solidified solute distribution predicted by present model and obtained from experiment [Kato and Cahoon, 1985].

region defined as negative segregation. At the advent of solidification, this negative segregation is confined only to the uppermost section of the mushy zone. However, with the progress in the solidification process, as the solid-mushy and mushy-liquid interface keeps moving in the upward direction, the region of negative segregation gradually engulfs the entire mushy region.

The reasonable match obtained from the validation of the present model concerning vertical solute concentration and temperature distribution (figure 5.2) establishes the robustness and reliability of the present model. The confidence in the present model being justified by this validation, we next endeavor to implement the model to investigate the binary alloy solidification associated with freckle formation under the combined influence of solutal convection and shrinkage induced flow in the next subsection.

5.4.2 Solidification of Al-30 wt.% Mg

For the case study associated with freckle formation under the combined influence of solutal convection and shrinkage induced flow, we have chosen Al-30 wt.% Mg as the model binary alloy. For this binary alloy system, Aluminum assumes the role of solvent, and Magnesium plays the role of solute. The motivation to choose Al-30 wt.% Mg as the model binary system for the

present study arises from the similarity of the phase diagram of Al-Mg alloy with $\text{NH}_4\text{Cl-H}_2\text{O}$ binary system, which is one of the most common model binary system deployed to study freckle formation phenomena [Chen and Chen, 1991; Chen et al., 1994; Chen, 1995; Peppin et al., 2008; Katz and Worster, 2008; Chakraborty and Dutta, 2013; Kumar et al., 2018a]. However, $\text{NH}_4\text{Cl-H}_2\text{O}$ binary system being subjected to volume expansion instead of shrinkage during liquid-solid phase transition process makes such a well studied system invalid for our current study involving shrinkage induced flow. For all the reported case studies involving freckling phenomena during the solidification of $\text{NH}_4\text{Cl-H}_2\text{O}$ binary system, the initial concentration (C_0) is chosen close to the eutectic composition [Chen and Chen, 1991; Chen et al., 1994; Chen, 1995; Peppin et al., 2008; Katz and Worster, 2008; Chakraborty and Dutta, 2013; Kumar et al., 2018a]. Apart from this, the Al-Mg alloy system having a large shrinkage ratio (ρ_s/ρ_l) is ideal for promoting shrinkage induce flow during the solidification process. Al-Si is another potential binary alloy system that we explored for this study considering the large value of shrinkage ratio (ρ_s/ρ_l) [Dagner et al., 2008]. However, owing to the smaller difference between the solubility in solid and liquid phases along with a much smaller value of solutal expansion coefficient β_C , Al-Si binary system is less prone to promote significant solutal instability leading to the formation of freckles [Willers et al., 2008]. Also, Al-Mg being a commonly used alloy system for various industrial applications, we chose this system as our model binary alloy. It is pertinent to mention here that the effect of micro-structure on permeability is not considered for the current study. Since the permeability linked with micro-structure in the mushy zone plays a key role in defining the freckling phenomena [Sarazin and Hellawell, 1988], the exclusion of the micro-structure effect in the present model is one of the major limitations of this study. However, the flow physics captured by the present study is expected to be valid whenever the micro-structure in the mushy region is conducive to promoting freckling phenomena. Hence, the results obtained from the study considering Al-30 wt.% Mg alloy as the model binary system can be considered to be consistent without losing any generality; and the physical understanding of the phenomena is equally applicable to any other binary system with favourable micro-structure in the mushy zone to promote freckle formation under the influence of shrinkage induced flow.

For the bottom cooling configuration, liquid to solid phase transition ensues from the bottom section of the cavity, causing rejection of lighter solute (Magnesium) in the adjacent melt. The presence of excess lighter solute (Magnesium) in the melt at the lower region of the cavity promotes instability of the solutal buoyancy field within the melt. When the instability of the solutal buoyancy field becomes strong enough to overcome the stably stratified thermal buoyancy field, free convection in the form of plumes ensues, causing the formation of channels in the mushy region [Sarazin and Hellawell, 1988; Felicelli et al., 1991]. For the present study, the alloy composition is initially maintained at a temperature $T_i = 770 \text{ K}$ (figure 5.3) which is approximately

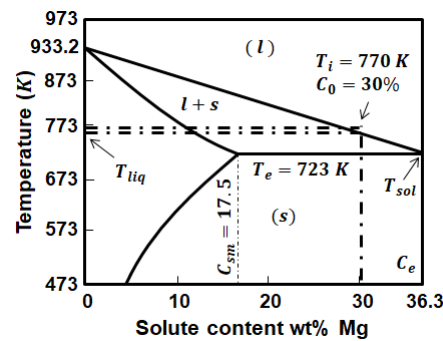


Figure 5.3 : Al (Solvent) - Mg (Solute) phase diagram till eutectic composition

10 K above the liquidus temperature corresponding to nominal magnesium composition ($C_0 = 30\%$). Solidification is attained by maintaining the bottom wall temperature below eutectic temperature (T_e at time $t > 0$ s). The initial set of studies associated with the grid dependence is performed by maintaining the bottom wall temperature 3 K below eutectic temperature ($T_e = 723$ K). The rejected solute (Mg) in the melt being lighter during the growth of solid front from the bottom, the solutal and thermal buoyancy fields oppose each other. While the effect of lighter solute rejection during solidification at the cavity bottom attributes to the density reduction of the local melt, the effect of low temperature (associated with the positive temperature gradient in the upward direction) on density is reverse at the cavity bottom [Sarazin and Hellawell, 1988; Felicelli et al., 1991]. One way to ensure density inversion at the cavity bottom is to enhance the instability of the solutal buoyancy field while suppressing the stable stratification effect of the thermal buoyancy field. The suppression of the thermal buoyancy effect can be attained by setting up an overall small temperature difference across the melt domain. For the present analysis associated with the grid independence study, the maximum value of the overall temperature difference is given by $T_i - T_c = 50$ K, where T_c represents the temperature of the cold bottom boundary. The phenomena of density inversion and freckle formation involving double-diffusive convection during alloy solidification in the bottom cooled configuration are extremely uncertain in nature due to the associated non-linearity of the problem. Obtaining grid and time-step independence for such a highly non-linear problem poses an enormous challenge [Sung et al., 2001; Guo and Beckermann, 2003; Sajja and Felicelli, 2011]. In the succeeding subsection, an attempt has been made to address the challenges associated with grid independence.

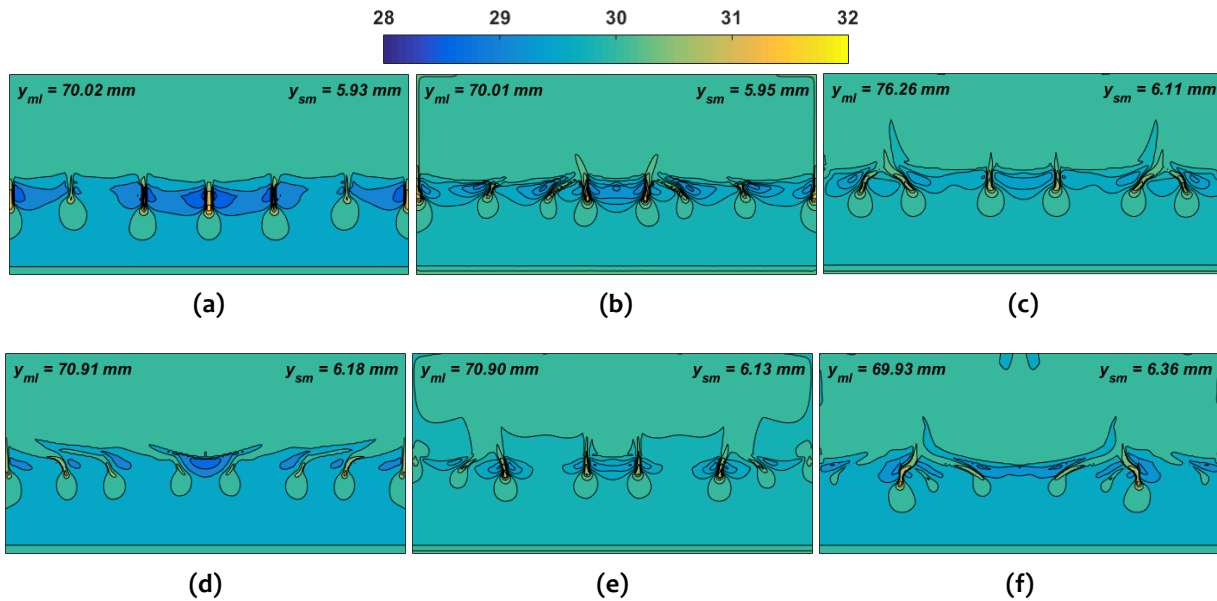


Figure 5.4 : Mesh sensitivity analysis: Solute composition distribution of Mg after 100 s time interval with varying grid and time step resolutions: (a) 60×60 and $\Delta t = 0.25$ s; (b) 90×90 and $\Delta t = 0.25$ s; (c) 120×120 and $\Delta t = 0.25$ s; (d) 150×150 and $\Delta t = 0.25$ s; (e) 150×150 and $\Delta t = 0.5$ s; and (f) 150×150 $\Delta t = 0.05$ s. y_{ml} and y_{sm} represent mushy-liquid and solid-mushy interface locations respectively estimated along symmetric axis.

5.4.3 Effect of grid size and time-step on numerical simulation

The solidification domain (figure 5.1) consists of a rectangular cavity of dimension 150×300 mm^2 with an opening of size 40 mm at the center of the top wall. As the computation is performed for one of the symmetric halves (150×150 mm^2), the opening size for the symmetric half is considered to be 20 mm. In order to investigate the effect of grid size on simulated predictions, bottom-up solidification of Al-30 wt.% Mg binary alloy, initially at pure liquid state at 770 K and subjected

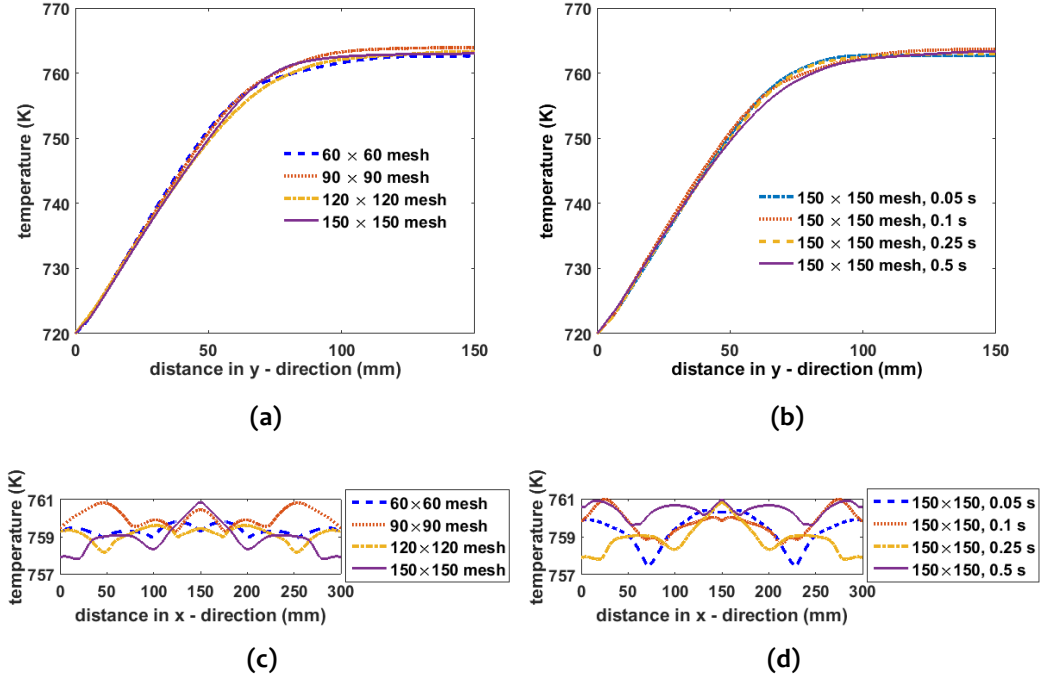


Figure 5.5 : Comparison of temperature profiles after 100 s time interval (a) along symmetry axis for varying grid resolution and $\Delta t = 0.25$ s; (b) along symmetry axis for varying time-step resolution and grid resolution 150×150 ; (c) along horizontal direction at a distance of $y = 80$ mm from bottom wall for varying grid resolution and $\Delta t = 0.25$ s; and, (d) along horizontal direction at a distance of $y = 80$ mm from bottom wall for varying time step resolution and grid resolution 150×150 .

to 720 K cold boundary condition at the bottom surface is considered. All other surfaces are considered to be perfectly insulated. The opening and the symmetry plane are subjected to symmetric thermal boundary conditions. For all the surfaces, the no-slip boundary condition is implemented for the velocity field, while the symmetry plane is subjected to symmetric velocity boundary conditions. Finally, zero gauge pressure boundary condition is implemented at the top opening for solving momentum conservation Eqns. 5.2 and 5.3. Analysis is carried out for four different grid resolutions namely: 60×60 , 90×90 , 120×120 , and 150×150 cells, and four different time-step resolutions namely: $\Delta t = 0.25$ s, $\Delta t = 0.5$ s, $\Delta t = 0.1$ s and $\Delta t = 0.05$ s. The number of cells or representative elementary volumes (REV) sharing their boundaries with the top-central opening are 8, 12, 16, and 20, respectively, for these four grid resolutions, respectively. For each grid resolution, the numerical simulation is carried out till 100 s to capture the evolution of temperature, velocity, concentration, and liquid-solid volume fraction field. Figure 5.4 shows the comparison of the Mg concentration field for four different grid resolutions and three different time-steps. Figure 5.4(a)-(d) represent Mg concentration fields obtained after 100 s with grid resolutions 60×60 , 90×90 , 120×120 , and 150×150 respectively, and time-step $\Delta t = 0.25$ s. Figure 5.4(d)-(f) represent the comparison of Mg concentration field when grid resolution is kept unaltered at 150×150 but three alternative time-steps, namely: $\Delta t = 0.25$ s, $\Delta t = 0.5$ s and $\Delta t = 0.05$ s are used. It is evident from this comparison that the dependence of simulation results on grid resolution and time-step is unavoidable even with a significantly large number of grids and smaller time steps. However, certain distinct features such as locations of plume (channel) formation, number of channels, solid-mushy (y_{sm}), and mushy-liquid (y_{ml}) interface locations showcase reasonably well-behaved similarities with increasing grid resolution. For instance, 90×90 , 120×120 , and 150×150 grid resolutions with time-step $\Delta t = 0.25$ s (figure 5.4(b)-(d)) showcase

fairly similar distribution of channels along with closely matching solid-mushy and mushy-liquid interface locations. The comparison of vertical temperature profile along the symmetry plane at 100 s is shown in figure 5.5(a)-(b), and the comparison manifests close resemblance with minimal difference between temperature profiles with varying grid and time-step resolutions. On the other hand, when the horizontal temperature profile just above the mushy-liquid interface is compared for different grid resolutions and time step resolutions (figure 5.5(c)-(d)), substantial variations between the temperature profiles can be observed. However, the range of temperature for these variations is found to be conveniently small (~ 3 K). Therefore, we conclude that obtaining simulation results with complete insensitivity to the grid and time-step resolution is unattainable for this case study. This observation is in line with the studies reported by Sung et al. [2001]; Guo and Beckermann [2003] and Sajja and Felicelli [2011]. Sung et al. [2001] studied the grid dependence for freckle formation in 2-D with Nickle base super-alloy and recommended the grid size relying on primary dendrite arm spacing and solute diffusivity in liquid. Guo and Beckermann [2003] performed 3-D grid dependence analysis with Pb-Sn alloy and concluded that the finer grid resolution is insufficient to achieve grid independence and is a cause of volatile behaviour of freckles formation over initial instabilities. Sajja and Felicelli [2011] employed fractional step adaptive meshing, which efficiently and accurately track the freckle formation, but reported two limitations concerning round-off errors and ill-conditioned boundaries (the continuity equation). From the present endeavour and other existing studies [Sung et al., 2001; Guo and Beckermann, 2003; Sajja and Felicelli, 2011] in the pursuit of achieving grid and time-step independence, it is clear that achieving complete independence from grid and time resolution will remain unresolved. Since high grid resolution and smaller time-steps demand significantly large computational time, we have restricted the grid resolution to 150×150 cells and time-step to 0.25 s for all the simulation results discussed in the forthcoming subsections. All the simulations are carried out on a Intel(R) Xenon(R) CPU E5-2650 v4 @ 2.20GHz computer and, for the 150×150 grid cells, required approximately 24-240 CPU seconds for each 1 s of real time simulation. The maximum total CPU time required to complete the simulation is approximately 25 hrs.

5.4.4 Effect of shrinkage induced flow on freckle formation

In the present subsection, the effect of shrinkage induced flow on freckle formation is analysed. Cavity geometry, boundary conditions, and initial condition are considered to be the same as the physical domain description in the previous subsection involving grid and time-step independence study. Figure 5.6, 5.7, and 5.8 represent the velocity field, liquid fraction and stream function, and species distribution within the rectangular cavity domain at different time intervals during the ongoing solidification process. As is evident from figure 5.6(a), 5.7(a) and 5.8(a), the melt convection in the cavity is predominantly developed due to the shrinkage effect at the initial stage of solidification (at $t = 20$ s), and density inversion due to the instability of solutal buoyancy field is absent during this stage. At the initial stage of solidification, volumetric shrinkage due to the solidification causes melt inflow into the cavity through the opening located at the top surface of the cavity giving rise to the circulation of melt adjacent to the opening. However, owing to the resistance posed by the stably stratified thermal buoyancy field, the incoming flow through the cavity opening cannot penetrate deeper into the cavity, and rather rerouted along the lateral direction having lesser flow resistance. Thus, at the initial stage of solidification, the interaction between the shrinkage induced flow and stably stratified thermal buoyancy field manifests a counter-intuitive flow reversal phenomena akin to the observations made by Monde et al. [2020] during the study involving bottom-up solidification of pure substance in a cavity with a central riser. As the solidification process progresses in time, solutal instability sets in near the mushy-liquid interface (figure 5.6(b), 5.7(b) and 5.8(b)) due to the rejection of excess lighter solute (Mg) in the melt caused by liquid to solid phase transition. The advent of solutal instability also leads to the onset of freckle formations in the mushy region. Coupled interaction between the shrinkage induced flow and solutal instability gives rise to complicated flow evolution in the melt

region (figure 5.6(b) and (c)) defining shape and orientation of the channels within the mushy region (figure 5.7(b) and (c)). The slanted orientation of channels shown in figure 5.7(c) and (d) can be attributed to this coupled interaction. As is evident from figure 5.8(c) and (d), the evolution of macro-segregation or species distribution is strongly influenced by the flow field. All the channel locations are characterized by positive segregation ($C > C_0$), while all the surrounding mushy regions are having negative segregation ($C < C_0$). With the further progress of the solidification process, the strength of the plumes gradually diminishes owing to the ever reducing height of the melt zone and natural closure of the channel openings into the melt region due to their slanted orientations. As the growth of the mushy region extends to approach the upper wall of the cavity, shrinkage induced flow reclaims its domination in the pure liquid and mushy region in the presence of very weak solutal influence (figure 5.6(d) and 5.7(d)). The effect of shrinkage induced flow on macro-segregation is distinctively manifested by a concentration distribution that resembles a stag-horn structure spreading symmetrically on both sides and centred around the symmetric plane (figure 5.8(d)).

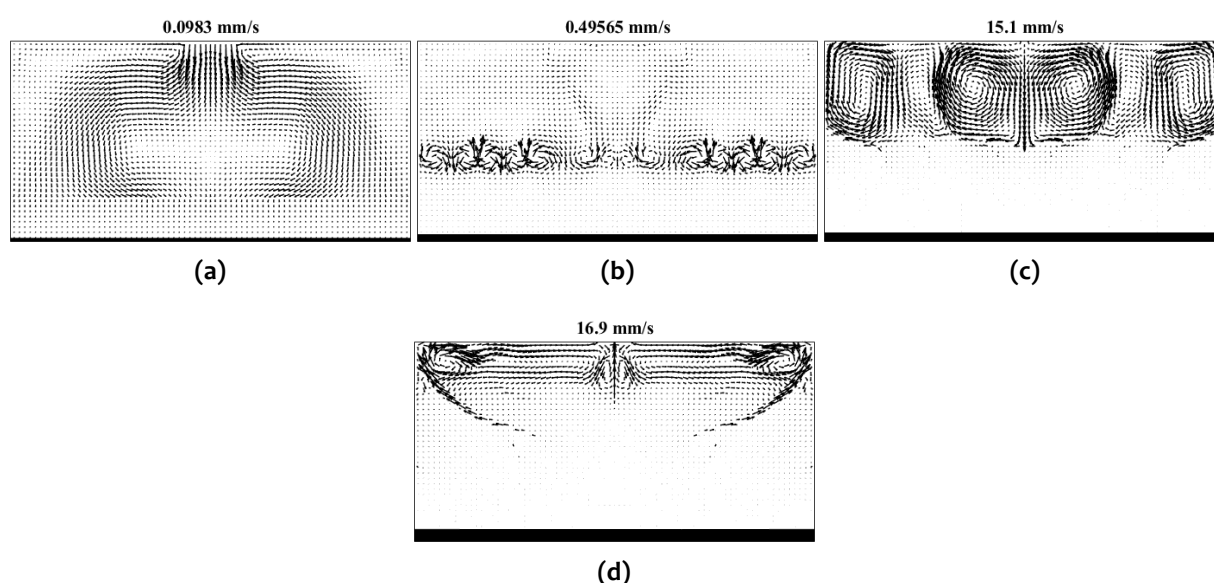


Figure 5.6 : Numerically predicted velocity field in the rectangular domain at different time intervals: (a) $t = 20\text{ s}$, (b) $t = 60\text{ s}$, (c) $t = 100\text{ s}$, and (d) $t = 200\text{ s}$. Magnitude of the maximum velocity within the domain is mentioned at the top of the individual figure.

5.4.5 Effect of inlet opening size on macro-segregation during freckle formation

The intensity of the shrinkage induced flow is expected to have a significant influence on the evolution of freckle orientation and macro-segregation. The prediction of the macro-segregation in the final cast product is of imminent interest in many manufacturing applications. Therefore, we endeavour to study the effect of shrinkage induced flow intensity on the final macro-segregation pattern in the cast product. The intensity of the shrinkage induced flow is highly dependent on the size of the opening for melt inflow into the cavity and the boundary condition at the bottom surface. In the present subsection, the study involves varying shrinkage induced flow intensity by means of varying the opening size, while the cold bottom boundary is maintained at the same constant temperature. The second part of the study involves varying cold boundary temperature for a fixed inlet opening size and will be discussed in the subsequent section.

For the varying opening size analysis, simulations are performed with six different inlet openings at the center of the top surface of the cavity viz. 16 mm, 30 mm, 40 mm, 60 mm, 150 mm, and fully open (300 mm). For all these cavity openings, the bottom wall temperature is maintained at 700 K. All the geometric parameters and initial condition, and other boundary conditions

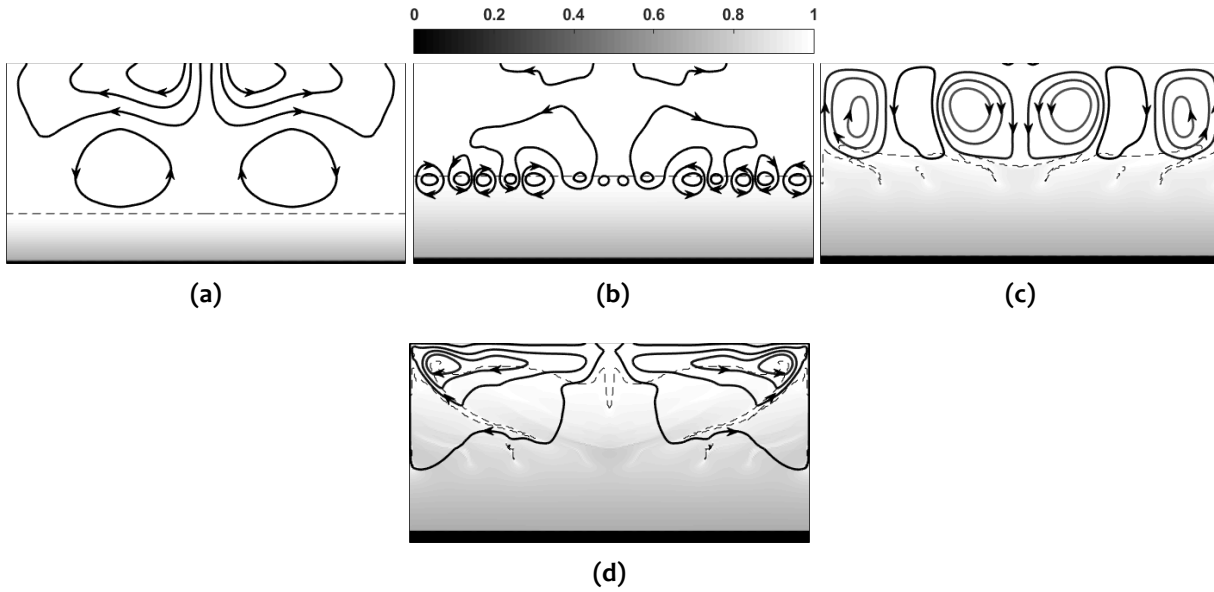


Figure 5.7 : Numerically predicted liquid fraction and stream function in the rectangular domain at different time intervals: (a) $t = 20 \text{ s}$ (b) $t = 60 \text{ s}$, (c) $t = 100 \text{ s}$, and (d) $t = 200 \text{ s}$. Dashed lines denotes the mushy-liquid interface

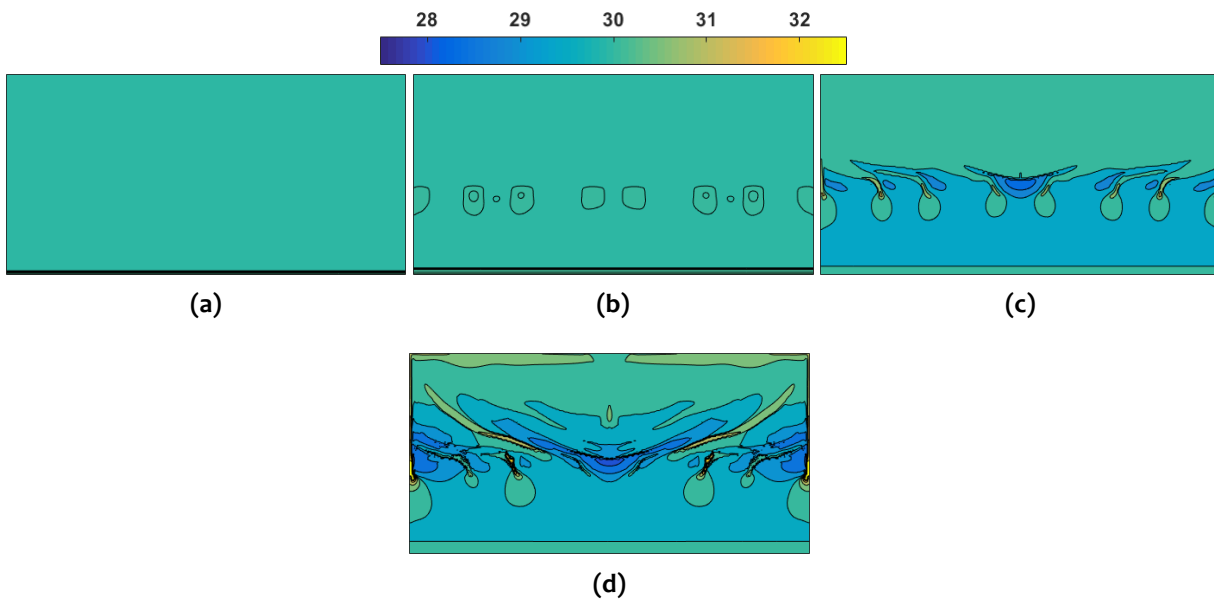


Figure 5.8 : Numerically predicted solute (Mg) distribution in the rectangular domain at different time intervals: (a) $t = 20 \text{ s}$ (b) $t = 60 \text{ s}$, (c) $t = 100 \text{ s}$, and (d) $t = 200 \text{ s}$.

are considered to be the same as those discussed in the preceding subsections. Unlike the case studies discussed in the preceding subsections (with bottom surface temperature 3 K below the eutectic temperature), the bottom wall temperature is purposefully chosen to be at a lower value (23 K below the eutectic temperature) to expedite the solidification process and to obtain faster completion of the solidification process in the cavity. Figure 5.9 and 5.10 shows the predicted concentration and velocity fields respectively for different inlet size openings obtained after the time interval 80 s . The simulation results indicate that the opening size has negligible influence over the onset of solutal instability and freckle formation, and for all different opening sizes, the solutal instability initiates almost after the same time interval. However, once the convection in

the form of plumes sets in, the concentration distribution and flow field in the melt domain is significantly sensitive to the opening size (figure 5.9 and 5.10). For smaller openings, although the shrinkage induced flow intensity is high along the symmetry line, most of the flow interactions with this incoming flow are restricted only with the nearest pair of neighbouring plumes adjacent to the symmetry line (figure 5.10(a) and (b)). As the opening size increases, the intensity of shrinkage induced flow reduces considerably. However, the zone of flow interaction is not restricted to a domain just adjacent to the symmetry line only. As a result, the weak incoming flow field through the opening interacts with more number of upcoming plumes resulting in significant alteration of the flow field at the upper half of the cavity (figure 5.10(c), (d) and (e)). When the entire upper surface of the melt is exposed to inflow, the intensity of shrinkage induced flow becomes extremely weak, and plume convection due to solutal instability dominates in the melt region (figure 5.10(f)). Although the shrinkage induced flow intensity is extremely weak for the completely open-top configuration, the effect of flow interaction is still perceivable from figure 5.10(f). Strong plumes moving in the upward direction around the cavity symmetry lines pose a strong resistance for the shrinkage induced flow to penetrate inside the cavity through the central portion of the opening. As a result, most of the shrinkage induced incoming melt through the opening is coerced to enter the cavity through the two corner sections of the opening. The effect of incoming melt flow through the opening corners is to suppress the plume formations in those regions and to bend stronger plumes at the two extremities toward the central region. Thus, the effect of opening size on the plume and channel formation can be comprehensively summarised as follows: (i) for small opening size, the shrinkage induced flow interacts mostly with the pair of immediately neighbouring plumes adjacent to the symmetry line (figure 5.10(a) and (b)); (ii) for moderate opening size, the effect of shrinkage induced flow expands laterally from the center-line, and more number of neighbouring plumes distributed around the central line interact with the incoming flow (figure 5.10(c), (d) and (e)); and finally, (iii) for very large opening size, the interaction of shrinkage induced flow is negligibly small with the plumes generated around the central symmetry line but having a significant contribution in the suppression of the corner plumes (figure 5.10(f)).

The plumes observed in present numerical study are similar to the results reported in literature [Jain et al., 2007; Chakraborty and Dutta, 2013; Sung et al., 2001]. The observed channels are purely developed due to solutal instability and has a point source of order 10^{-4} m, which have been perceived both numerically [Jain et al., 2007; Chakraborty and Dutta, 2013] and experimentally [Kumar et al., 2018a]. However, the classic plume structures formed by localized heating are quite different from present plume structure. These classic plumes are generally observed with periodic puff and bulge that corresponds to instability of lapping flow [Hattori et al., 2013; Lopez and Marques, 2013]. In thermally driven plumes, the surrounding ambient is at a temperature lower than the heating source placed at the bottom. Due to the thermal instability, buoyancy force directs the lighter fluid present near the hot source in upward direction. The disturbance observed on the surface of thermally driven plume is developed due to dynamic interaction of surrounding fluid with the plume. Particularly when the plume has a point source, the disturbance augments as the density difference between the surrounding and plume reduces [Yang, 1992] leading to sinusoidal disturbance. In the present study, plume sources are similar to point source and caused by marginal change in solute concentration. Therefore, the situation is conducive of promoting sinusoidal disturbance rather than periodic puffing and bulging phenomena.

Further, Figure 5.11(a)-(f) shows a comparison of the final macro-segregation after the completion of the solidification process in the cavity for different inlet opening sizes. It is evident from these results that macro-segregation and freckles formation has a strong dependence on the evolving velocity distribution owing to the interaction between shrinkage induced flow and solutal instability. The final macro-segregation pattern around the symmetry field distinctively resembles a wide variety of ram-head pattern (figure 5.11(a)-(f)). In an earlier instance (figure 5.8(d)), at an

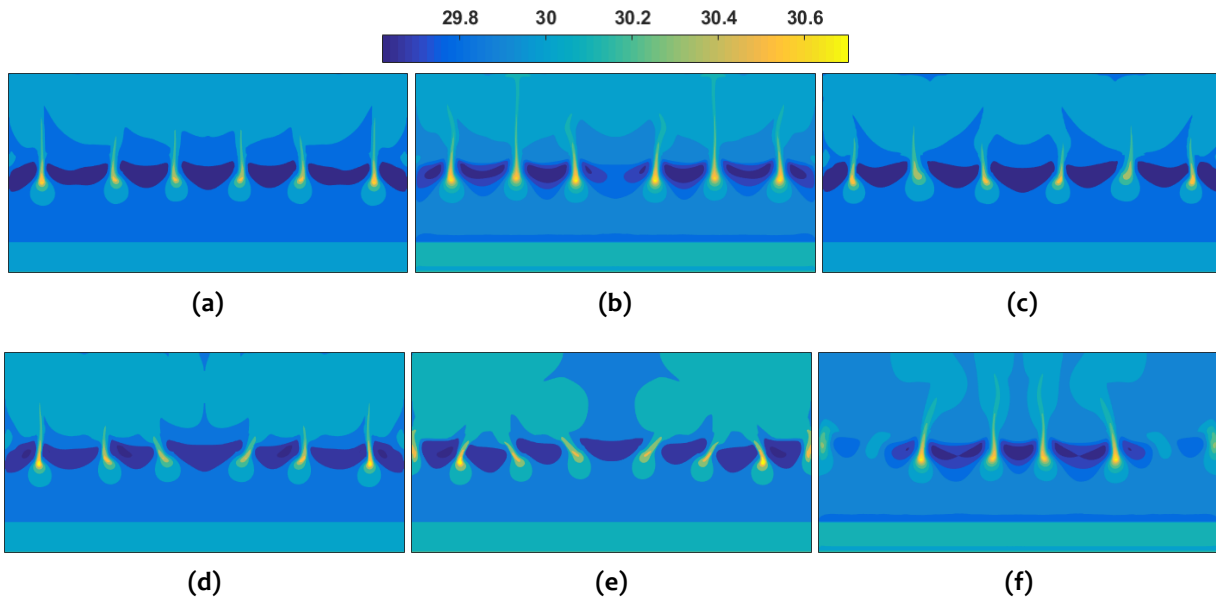


Figure 5.9 : Numerically predicted solute (Mg) distribution in the rectangular domain for different inlet openings sizes at $t = 80$ s: (a) 16 mm, (b) 30 mm, (c) 40 mm, (d) 60 mm, (e) 150 mm, and (f) 300 mm.

intermediate stage of solidification in the cavity with an opening size of 40 mm and bottom surface temperature 720 K, we came across a similar (stag-horn) segregation pattern. For the cases with smaller openings, the severe solute lean regions are observed adjacent to the opening at the top surface owing to the inflow of liquid melt with a nominal composition (C_0) into the mushy regions in those locations (figure 5.11(a)-(d)). On the other hand, for large opening sizes (figure 5.11(e)), this severely solute lean locations are shifted toward the opening corner sections. For a fully open top surface, mild entrainment of severely negative segregation is observed at the central and lateral locations adjacent to the open surface (figure 5.11(f)). This mild entrainment of severely solute lean regions can be attributed directly to the very low intensity of shrinkage induced flow for this particular case. To substantiate the significance of shrinkage effect over the channel formation and macro-segregation, simulation is also performed without considering the shrinkage induced flow, and the macro-segregation obtained after the completion of the solidification process is depicted in figure 5.11(g) for comparison. As is evident from this comparison, the macro-segregation pattern without considering shrinkage induced flow is found out to be distinctively different from those involving the influence of shrinkage induced flow.

5.4.6 Effect of cold boundary temperature on macro-segregation

Next, we analyse the effect of cold boundary temperature on the final macro-segregation. For this particular set of case studies, the opening size at the center of the cavity top surface is kept fixed at 40 mm. Final macro-segregation patterns for three different cold boundary temperatures namely: 700 K, 623 K, and 523 K are presented in figure 5.12(a)-(c). In order to show the effect of cold boundary temperature on macro-segregation, we have purposefully chosen these cold boundary temperatures representing moderate, low, and very low cold boundary ($T_c = 700$ K, 623 K and 523 K respectively) at the bottom surface. Only when the unstable solutal buoyancy field overpowers the stably stratified thermal buoyancy field in the melt region, the solutal instability sets in, causing the onset of plume formation. Therefore, the onset of plume formation is essentially decided by the temperature, and solutal gradients along the vertical direction in pure melt region bounded at its lower end by the liquid-mushy interface. The growth rate of the mushy-liquid interface is directly related to the extent of cooling at the bottom surface. The lower the cold temperature at the bottom surface faster is the growth rate of the mushy-liquid interface and vice

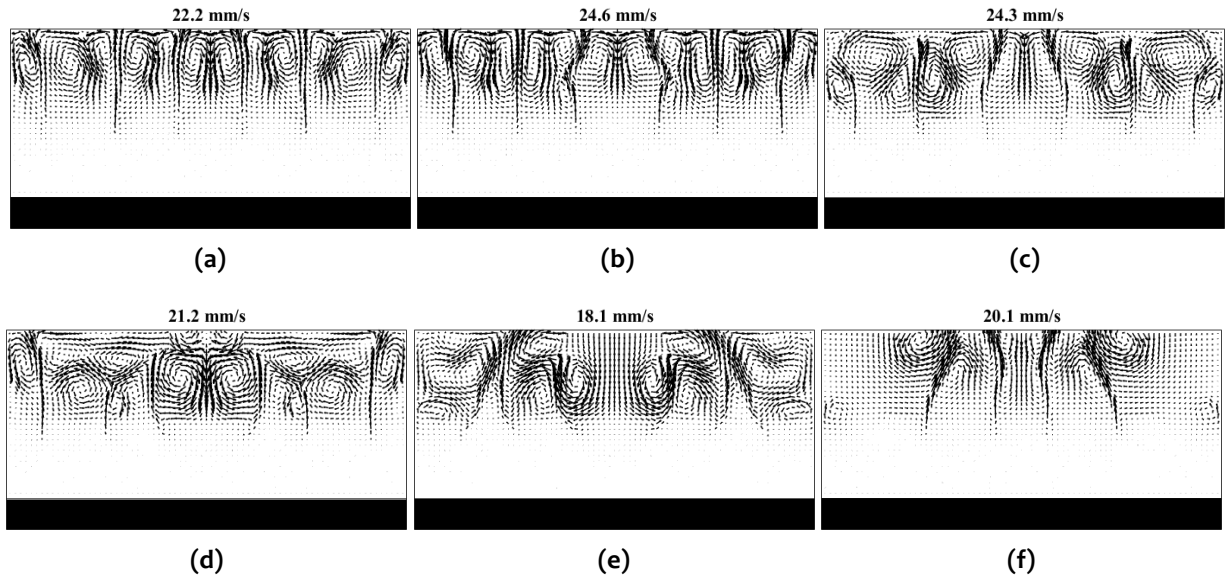


Figure 5.10 : Numerically predicted velocity field in the rectangular domain for different inlet openings sizes at $t = 80$ s: (a) 16 mm, (b) 30 mm, (c) 40 mm, (d) 60 mm, (e) 150 mm, and (f) 300 mm. Magnitude of the maximum velocity within the domain is mentioned at the top of the individual figure.

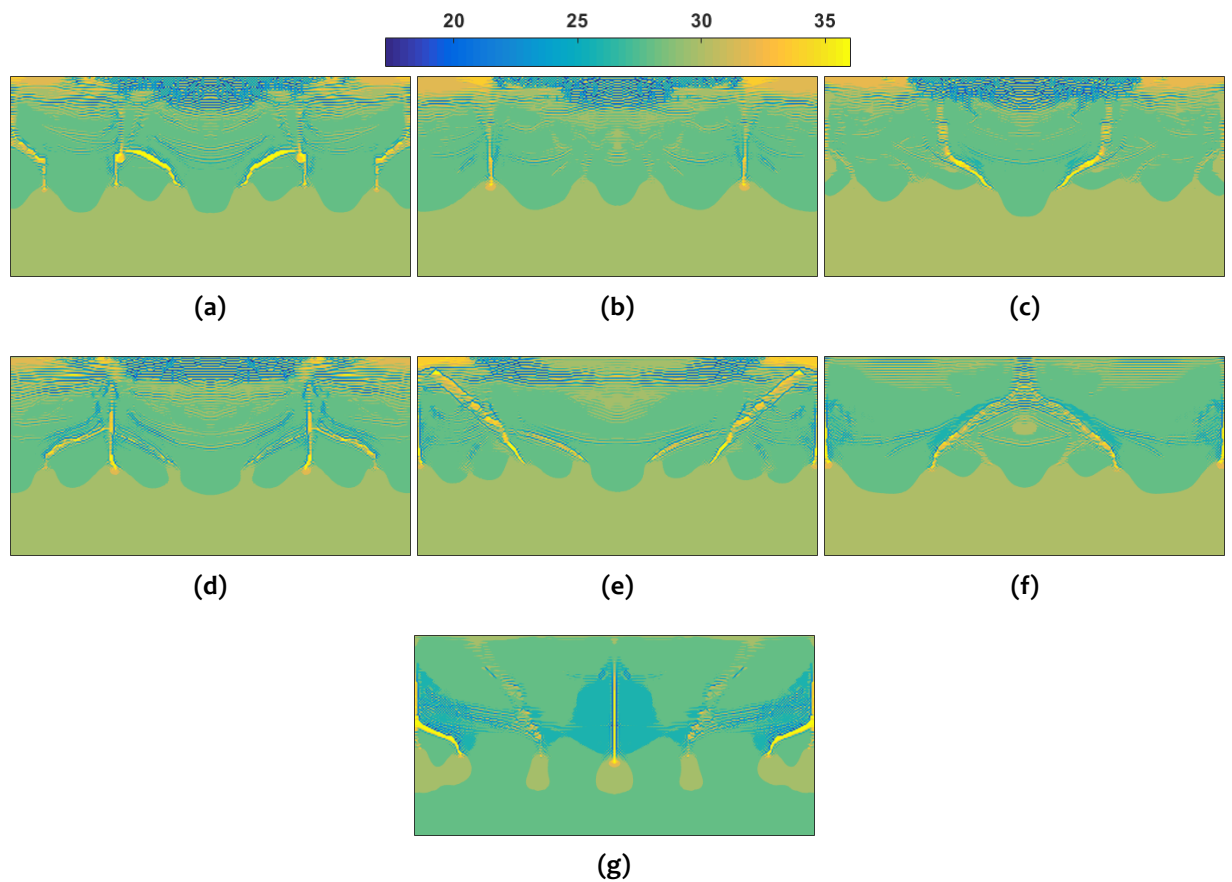


Figure 5.11 : Numerically predicted macro-segregation after the completion of the solidification process in the cavity for different inlet openings sizes: (a) 16 mm, (b) 30 mm, (c) 40 mm, (d) 60 mm, (e) 150 mm, (f) 300 mm, and (g) a case without considering the effect of shrinkage ($\rho_s = \rho_l = 2190 \text{ kg/m}^3$) for 300 mm opening size.

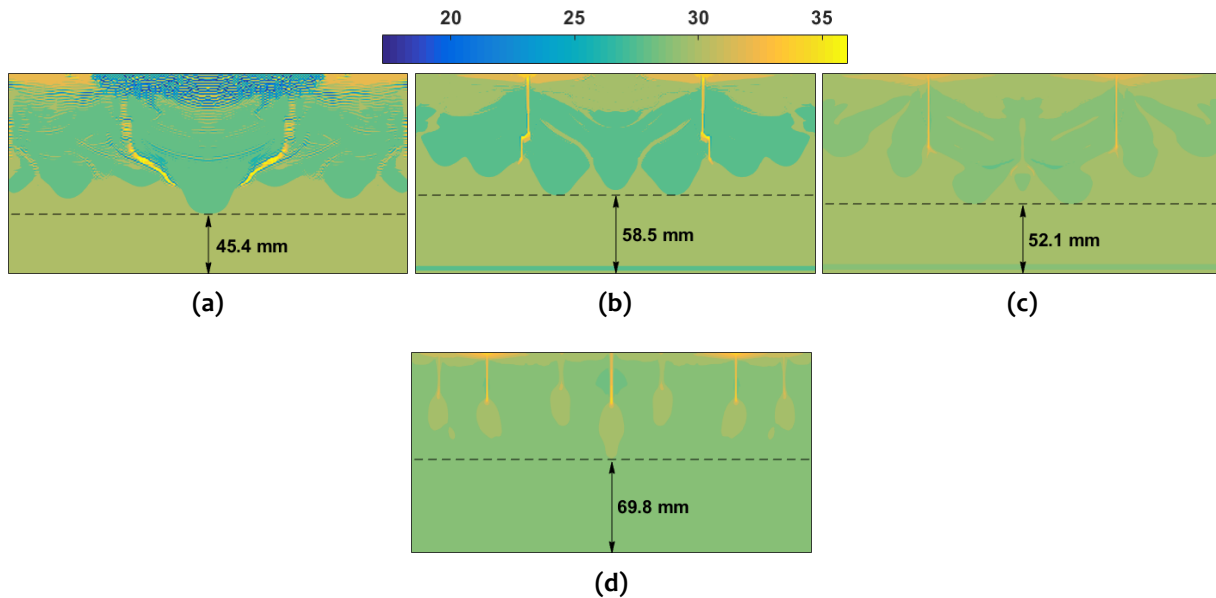


Figure 5.12 : Numerically predicted macro-segregation after the completion of the solidification process in the cavity for varying cold boundary temperatures: (a) $T_c = 700\text{ K}$, (b) $T_c = 623\text{ K}$, (c) $T_c = 523\text{ K}$, and, (d) a case without considering the effect of shrinkage ($\rho_s = \rho_l = 2190\text{ kg/m}^3$) for $T_c = 523\text{ K}$.

versa. When we compare final macro-segregation patterns for 700 K and 623 K cooling at the bottom surface (figure 5.12(a) and (b)), we find that the effect of channel formations are confined to a narrower thickness band at the upper portions of the cavity for the lower cooling. The net effect of lowering the cold surface temperature at the bottom is to shift the freckles formation in the upward direction to a small extent. The lowermost extent of ram-head protrusion (figure 5.12(a) and (b)) of the macro-segregation pattern signifies the onset of solutal instability. In terms of the growth rate of the mushy-liquid interface, the mushy-liquid interface moves further up for low cold temperature (623 K) as compared to moderate cooling (700 K) before solutal instability sets in. However, this upward shifting trend of freckles formation does not prevail as we bring down the cold temperature further down till we attain a very low cold temperature of 523 K (figure 5.12(c)). Not only the macro-segregation pattern for very low cold temperature (figure 5.12(c)) shows a distinct deviation from those depicted for moderate and low cold temperature (figure 5.12(a) and (b)), the effect of freckles formation is also spread over a broader thickness band at the upper portion of the cavity, indicating the onset of solutal instability at an early stage of solidification process. This early onset of solutal instability for very low cold temperature is truly intriguing and demands a feasible explanation. The very first idea that propels us to justify this highly non-intuitive feature is that it must be something to do with the effect of shrinkage induced flow. To confirm this notion, we performed another simulation considering the same very low cold temperature cooling (523 K) for the same system without considering the shrinkage effect and compared the macro-segregation (figure 5.12(d)). The comparison between figure 5.12(c) and (d) clearly confirms that the shrinkage induced flow indeed plays a key role in instigating early onset of freckle formation for very low cold temperature. The depth of the freckle-linked macro-segregation band is distinctively narrower when shrinkage induced flow is not taken into account (figure 5.12(c) and (d)). The early onset of solutal instability is attributed to the perturbation of the meta-stable solutal buoyancy field adjacent to the mushy-liquid interface by the shrinkage induced flow current coming down from the riser opening. The strength of shrinkage induced downward flow current is highly dependent on the extent of cooling at the bottom surface. The lower the cold temperature, the faster is the solidification rate, and the stronger is flow current entering the cavity through the central opening at the top surface to compensate for the reduced volume due to solidification. When the cold temperature is substantially low, the incoming shrinkage induced flow penetrates deep enough into the melt domain to perturb the meta-stable solutal buoyancy field adjacent to the mushy-liquid

interface. This perturbation causes the solutal instability to set in just around the line of symmetry. The meta-stable buoyancy field adjacent to the mushy-liquid interface is characterized by the presence of distinct solute rich zones along with this interface. The horizontal distribution of solute just above the mushy-liquid interface clearly demonstrates these local solute rich zones with distinct peaks of solute concentration (figure 5.13). These solute rich zones can be directly identified to be the possible plume sites. The coexistence of such solute concentration peaks along with positive peaks of vertical velocity components (of the range of $\sim 0.8-1.5 \text{ mm/s}$) is identified as the onset of solutal instability (figure 5.13). An example for the same is presented in figure 5.13, where onset is obtained for the case with 40 mm opening and cooling of 700 K . Figure 5.14(a) and (b) shows the onset of this solutal instability adjacent to the central plane of symmetry for 523 K cold temperature at the bottom surface. With the passage of time, this instability around the central symmetry line propagates in the lateral direction establishing new plume formation sites away from the central symmetry line (figure 5.14(c)-(d)). To emphasize the significance of the shrinkage induced flow strength as the major driving factor of the early onset of solutal instability, the flow pattern (figure 5.14(a)) obtained during the onset of plume formation for 523 K cold temperature at the bottom surface is compared with those obtained for 623 K and 700 K cooling (figure 5.14(e) and (f)). Figure 5.14(e) and (f) clearly shows that unlike 523 K cold boundary, solutal instability simultaneously sets in at several locations along with the mushy liquid interface. However, the interspace between the subsequent plume onset locations is much smaller for 623 K cold boundary (figure 5.14(e)) as compared to 700 K cold boundary (figure 5.14(f)). The key observations from this study can be consolidated as follows: (i) larger cooling promotes stronger shrinkage induced flow current to penetrate deeper into the melt region adjacent to the central symmetry plane, (ii) the stronger the shrinkage induced flow current, the narrower is the region of solutal instability around the central plane of symmetry with smaller interspace between subsequent plume locations, and, (iii) substantially large cooling by lowering the cold temperatures, triggers the early onset of solutal instability both in terms of time scale as well as the height of mushy-liquid interface.

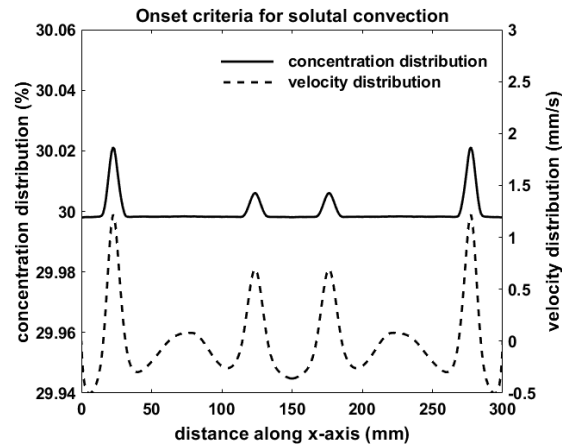


Figure 5.13 : Onset criteria defined by co-existing peaks in horizontal concentration distribution and vertical velocity component distribution near the meta-stable buoyancy field adjacent to the mushy-liquid interface for the case study with 40 mm inlet opening size and 700 K cold boundary.

Another interesting fact revealed by the comparison of macro-segregation patterns presented by figure 5.12(a)-(c) is associated with the severity of composition distribution in terms of the difference between the maximum and minimum concentration of Mg. A close look at the color bar representing the solute concentration scale in conjunction with the color-map representation of Mg concentration field in figure 5.12 clearly shows that moderate cooling at the bottom surface ($T_c = 700 \text{ K}$) gives rise to a much severe segregation denoted by $(C_{max} - C_{min}) \sim 19\%$ (figure 5.12(a)). For $T_c = 623 \text{ K}$ (figure 5.12(b)), $(C_{max} - C_{min})$ value is much smaller ($\sim 12\%$) and for $T_c = 523 \text{ K}$ (figure 5.12(c)), $(C_{max} - C_{min})$ value is even smaller ($\sim 6\%$). This ever-decreasing $(C_{max} - C_{min})$ value

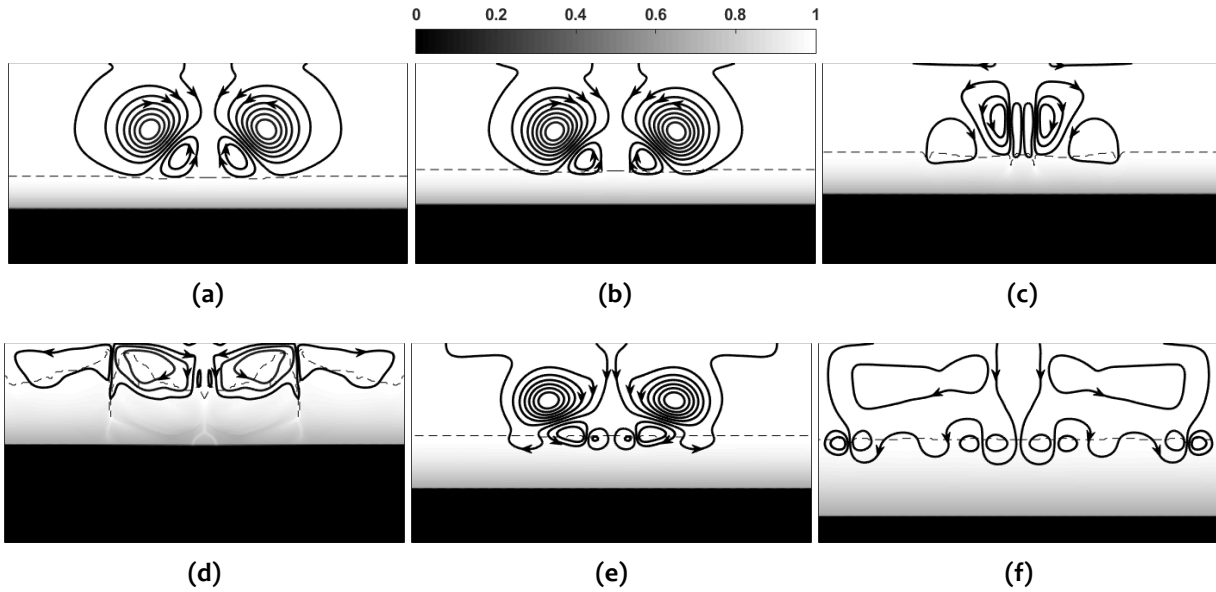


Figure 5.14 : Numerically predicted liquid fraction and stream function for constant inlet opening size of 40 mm at : (a) $t = 25$ s, $T_c = 523$ K (b) $t = 29$ s, $T_c = 523$ K (c) $t = 40$ s, $T_c = 523$ K (d) $t = 80$ s, $T_c = 523$ K (e) $t = 49$ s, $T_c = 623$ K and (f) $t = 62$ s, $T_c = 700$ K. Early onset of solutal instability is observed for significantly low cold temperature corresponding to $T_c = 523$ K.

with progressively lower cold temperature can be directly connected to the relative thickness of the mushy regions. For low cold temperature at the bottom surface, the pure liquid and pure solid region are separated by a thinner layer of the mushy region. On the other hand, a moderate temperature at the bottom surface gives rise to a comparatively thicker mushy layer separating the pure liquid and solid phases. It is the growth rate of the pure solid region that dictates the inflow of melt with a nominal composition (C_0) through the cavity opening at the top. The thinner mushy region associated with lower cold temperature at the bottom surface allows the incoming melt with a nominal composition (C_0) through the cavity opening to interact and mix with the pure melt at the upper region of the cavity for a substantial duration of the solidification process before the upper bound of the mushy layer is extended till the top surface of the cavity. On the other hand, when a moderate cold temperature is applied at the bottom surface, the upper bound of the mushy layer extends till the top surface at a much earlier stage of the solidification process bounded at the bottom by a slowly growing solid-mushy interface. As a result, the inflow of the melt through the opening at the top surface needs to percolate through the porous mushy region as the pure solid domain slowly extends in the upward direction. The flow resistance of the porous mushy layer does not allow free mixing of incoming melt from the cavity opening with the rest of the liquid distributed in the mushy layer. Owing to the continuous supply of fresh melt with a nominal solute composition (C_0) from the cavity opening, solute rich liquid phase due to liquid-solid phase transition is flushed out from the mushy region adjacent to the cavity opening and is distributed in the neighbouring mushy domain. The combined effect of prolonged shrinkage induced flow through porous mushy region along with a continuous supply of solute lean melt from the cavity opening till the completion of solidification causes severe negative segregation adjacent to this region when moderate cold temperature (figure 5.12(a)) corresponding to 700 K cooling) is applied at the bottom surface. However, the severity of this negative segregation perishes drastically for lower values of cold boundary at the bottom surface (figure 5.12(b) and (c)). Ram-head type segregation pattern around the symmetry plane prevails for $T_c = 700$ K and 623 K. However, the size of the ram-head type segregation around the central plane shrinks with decreasing cold boundary temperature. At $T_c = 523$ K, the downward protrusion along the central

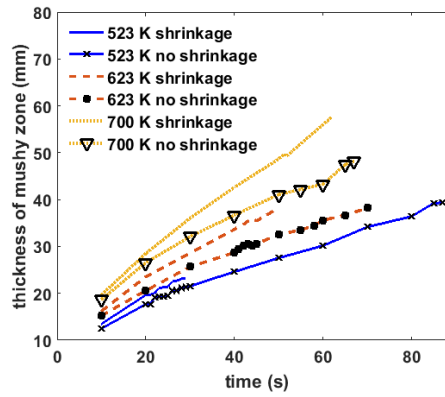


Figure 5.15 : Comparison of the time evolution of mushy layer thickness in the presence and absence of shrinkage induced flow for varying cold boundary temperature (T_c), before the solutal instability sets in.

plane almost vanishes, leaving a small trail of an isolated spot with negative segregation, and the overall effect is a macro-segregation pattern resembling a butterfly around the central plane.

Before concluding the findings from the case study associated with the effect of cold boundary temperature on the freckles formation and macro-segregation under the influence of shrinkage induced flow, we would like to highlight few more interesting observations. The first one among them is concerning the growth rate of the mushy region. It is evident from all the simulation results that the incorporation of shrinkage induced flow enhances the growth rate of the mushy layer. In figure 5.15 evolution of the mushy layer thickness with time is presented for three different cold boundary temperatures. The mushy-liquid and solid-mushy interface locations are monitored until the solutal instability sets in because the mushy-liquid interface has a planer growth till the advent of this event. The time evolution of mushy layer thickness obtained from the simulations involving shrinkage induced flow are compared with those obtained from simulations without considering shrinkage induced flow. As is evident from figure 5.15, for each of the assigned cold boundary temperatures, the mushy layer is predicted to be thicker whenever the effect of shrinkage induce flow is incorporated. The thicker mushy layer perceived by the model involving shrinkage induced flow can be explained as follows. The shrinkage induced flow allows continuous inflow of fresh melt (with nominal composition C_0) to interact and mix with the existing melt inside the cavity. The shrinkage induced flow being conducive to better mixing of melt within the cavity causes the dilution of otherwise solute rich melt adjacent to the mushy-liquid interface. Following the phase diagram (figure 5.3), dilution of solute concentration is coherent with the rise in local liquidus temperature. Thus the increase in local liquidus temperature caused by the dilution of solute concentration adjacent to the mushy-liquid interface promotes faster growth of the mushy region when shrinkage induced flow is taken into account. On the other hand, in the absence of shrinkage induced flow, the pure melt region remains quiescent until the onset of solutal instability. Owing to the negligibly small solutal diffusivity $\mathcal{D}(\sim 10^{-9}m^2/s)$ and absence of convective mixing mechanism prior to the onset of solutal instability, a solute rich melt layer builds up adjacent to the mushy-liquid interface. The solute rich melt adjacent to the mushy-liquid interface having a lower liquidus temperature hinders the growth rate of the mushy layer. One more important observation from figure 5.15 is associated with the onset timing of solutal instability. For all the assigned cold boundary temperatures (700 K, 623 K, and 523 K) in figure 5.15, we find that onset of solutal instability sets in at an earlier time instant whenever shrinkage induced flow is accounted for. As has been mentioned earlier, this early onset of solutal instability can be attributed to the perturbation of the meta-stable solutal buoyancy field adjacent to the mushy-liquid interface by the shrinkage induced flow combined with a faster growth rate of the mushy-liquid interface.

Next, the onset timings of solutal instability and the mushy-liquid interface locations

associated with this onset for a range of cold boundary temperature are compared for simulation results involving the presence and absence of shrinkage induced flow. Figure 5.16(a) shows that for the entire range of cold boundary temperature under consideration, the shrinkage induced flow causes early onset of solutal instability. The lower the cold boundary temperature earlier is the onset of solutal instability compared to no-shrinkage induced flow assumption. In terms of the mushy-liquid interface location, the solutal instability sets in at a comparatively lower height of the interface for no-shrinkage induced flow assumption when cooling at the cold boundary is moderate (corresponding to $T_c = 700\text{ K}$ and 673 K). However, with lower and lower cold temperature ($T_c = 623\text{ K}$, 573 K , 523 K and 300 K) a reverse trend sets in. Lower cold temperature intensifies the shrinkage induced inflow of melt into the cavity. Lower the cold temperature, the deeper is the penetration of the shrinkage induced inflow into the melt region. As a result, perturbation of the meta-stable solutal buoyancy field adjacent to the mushy-liquid interface by the shrinkage induced incoming flow occurs at progressively lower heights of mushy-liquid interface location with lowering the cold temperature. Since the time-scale to attain complete solidification in the cavity and interface growth rates is directly connected with the cold boundary temperatures at the bottom surface, representation of the onset of the solutal instability with respect to a normalized time scale and a normalized mushy-liquid interface location is much more desirable. In figure 5.16(b), the onset of the solutal instability is presented with respect to the normalized time-scale and normalized mushy-liquid interface location for six different cold boundary temperatures. The normalized time-scale (t^*) is obtained by dividing the dimensional time with the total time required to attain the complete solidification in the cavity ($t^* = t/\Delta t_{tot}$). Similarly the normalized mushy-liquid interface location (H^*) is defined as the ratio of mushy-liquid interface height ($H_{i(m-l)}$) to the cavity height (H_C), and is given by $H^* = H_{i(m-l)}/H_C$. For all the assigned values of cold boundary temperature, simulations pertaining to shrinkage induced flow are found to promote early onset of plume formation as compared to those in the absence of shrinkage induced flow when the onset is plotted against normalized time-scale. With increasing degree of cooling at the bottom surface ($T_c = 623\text{ K}$, 573 K , 523 K and 300 K) the normalized onset timing involving shrinkage induced flow is fairly insensitive to the cold boundary temperature, i.e. dt_{onset}^*/dT_c is very small. However, in the absence of shrinkage induced flow, the normalized onset timing is highly sensitive to the cold boundary temperature for the entire range T_c with large t_{onset}^* Vs. T_c slope. As is evident from figure 5.16(b), t_{onset}^* increase monotonically with decreasing T_c in the absence of shrinkage induced flow, while t_{onset}^* associated with shrinkage induced flow manifests an asymptotic behavior for the same indicating early onset of plume formation. Therefore, we can conclude that the shrinkage induced flow expedite the onset of solutal instability substantially for low cold boundary temperature at the bottom surface. Next, we verify the onset of plume formation with respect to the normalized mushy-liquid interface location (figure 5.16(b)). For moderate values of cold temperature at the bottom surface ($T_c = 700\text{ K}$ and 673 K), the height of normalized mushy liquid interface corresponding to the onset of plume formation (H_{onset}^*) is found to be lower when shrinkage induced flow is not considered. The reason behind this outcome can be attributed to the faster growth rate of the mushy layer associated with shrinkage induced flow. For instance, the difference between the normalized onset time instant corresponding to $T_c = 700\text{ K}$ is smallest for case studies associated with and without the consideration of shrinkage induced flow, but the normalized mushy-liquid interface height (H_{onset}^*) corresponding to shrinkage induced flow consideration is found to surpass the one obtained without shrinkage induced flow. As we keep decreasing T_c , the same trend prevails till some range of T_c ($T_c = 673\text{ K}$). With decreasing T_c values, the onset time lag between these two cases (without and with shrinkage induced flow) becomes more and more evident. However, the gap between the onset locations in terms of normalized mushy-liquid interface heights diminishes, leading to a cross over point below $T_c = 673\text{ K}$. After this cross over point, solutal instability stimulated by shrinkage induced flow sets in at progressively lower heights of normalized mushy-liquid interface locations (H_{onset}^*) as T_c is decreased further and further. This trend is completely contrary to the

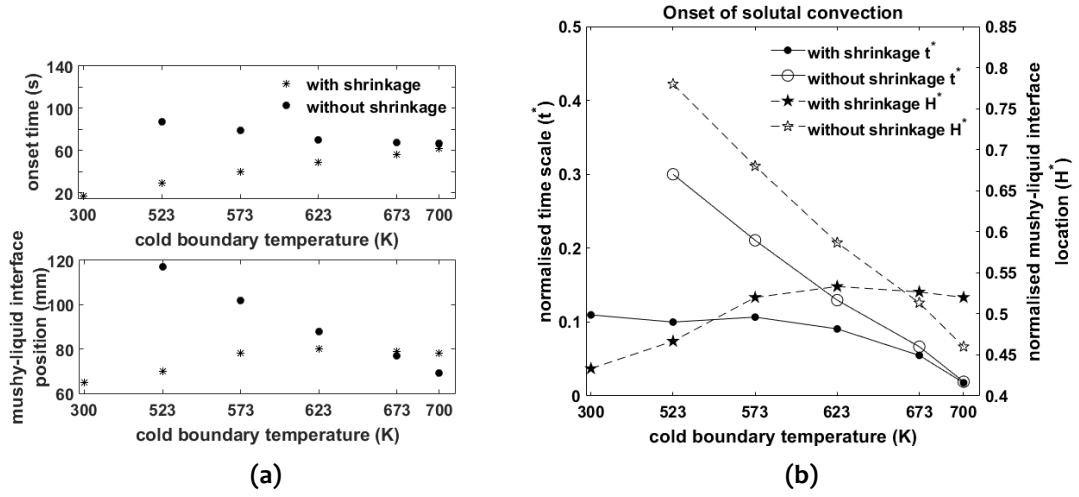


Figure 5.16 : Comparison of the onset time and associated height of mushy-liquid interface of solutal instability in the presence and absence of shrinkage induced flow for varying cold boundary temperature (T_c). (a) Dimensional representation of onset time and mushy-liquid interface height, and, (b) Normalized representation of onset time and mushy-liquid interface height.

ever-increasing H_{onset}^* behavior with progressively smaller values of T_c in the absence of shrinkage induced flow.

The results concerning the early onset of solutal instability (figure 5.16) associated with low cold temperature compelled us to revisit the effect of opening size on the onset phenomena once more. During the previous study considering cold boundary temperature to be at 700 K, we found the effect of opening size on the onset time and location to be negligible. Since smaller opening size enhances the strength of shrinkage induced flow, a similar outcome described by figure 5.16 should have been observed. Therefore, the insensitivity of the onset of solutal instability with respect to the inlet opening size at $T_c = 700 K$ should be justified. The intensity of shrinkage induced flow is directly dependent on the growth rate of the pure solid front; and the growth rate of the pure solid front has a direct correspondence with the extent of cooling at the bottom surface. For moderate cooling (with temperature at $T_c = 700 K$) the growth rate of pure solid front is significantly smaller than that obtained for very large cooling (temperatures at or below $T_c = 523 K$). Therefore, the intensity of shrinkage induced flow is expected to be much larger for very low cold temperature as compared to moderate cold temperature. Also, the effect of inlet opening size on the onset of solutal instability should be much more prominent when very low cold temperature case is considered. Figure 5.17 shows the effect of varying inlet opening size on the onset of solutal instability for three different cold boundary temperature (T_c) viz. 700 K, 523 K and 300 K. And indeed, we find the onset of solutal instability to be significantly sensitive to the inlet opening size for $T_c = 523 K$ and $T_c = 300 K$ (figure 5.17); particularly when the opening size varies from 40 mm to 10 mm. However, we encounter a very strange feature of the onset profile on the normalised time and mushy-liquid interface length scale for $T_c = 523 K$ and $T_c = 300 K$, when the inlet opening size is reduced from 20 mm to 10 mm. As we keep on decreasing the opening size till 20 mm, t^* and H^* corresponding to the onset of solutal instability reduce monotonically signifying early-onset phenomena. But the reduction of the opening size below 20 mm upsets this monotonic trend drastically, featuring onset delay with higher values of t^* and H^* . Thus, it is necessary to justify the cause of this onset delay as the inlet opening size is reduced below 20 mm.

As mentioned earlier, the onset sites for plume formation are closely associated with the regions along the mushy-liquid interface, where the accumulation of high solute concentration sets in representing the meta-stable concentration field (figure 5.13). Weaker shrinkage induced flow associated with moderate cold temperature at the bottom surface and larger inlet opening size does not penetrate the mushy region and gets dissipated solely within the pure melt region. However,

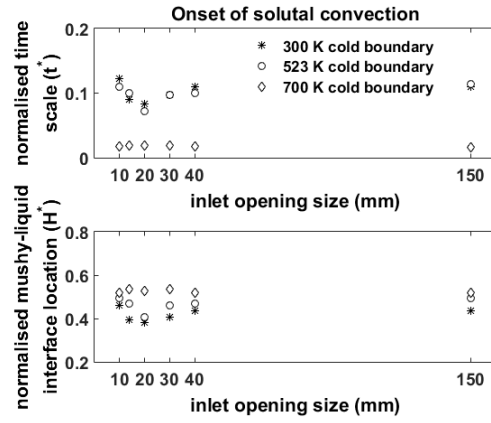


Figure 5.17 : Normalized representation of onset times and associated mushy-liquid interface heights of solutal instability for varying inlet opening size, viz. 10 mm, 14 mm, 20 mm, 30 mm, 40 mm, and 150 mm, for $T_c = 700\text{ K}$, $T_c = 523\text{ K}$ and 300 K .

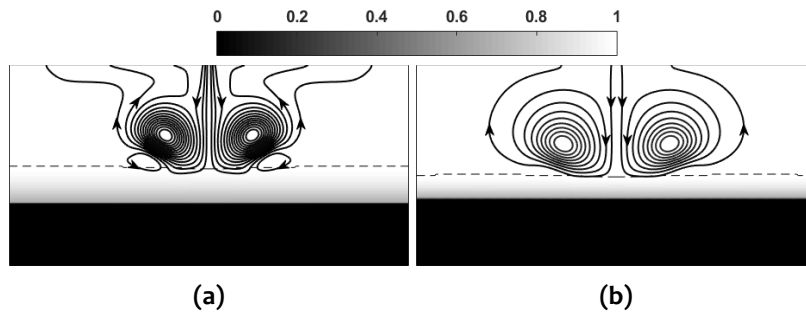


Figure 5.18 : Numerically predicted liquid fraction and stream function at the onset of solutal instability (a) $t_{onset} = 32\text{ s}$ and $T_c = 523\text{ K}$; (b) $t_{onset} = 19\text{ s}$ and $T_c = 300\text{ K}$ for 10 mm inlet opening size

the slight perturbation of the meta-stable solutal field adjacent to the mushy-liquid interface caused by this weak shrinkage induced flow gives rise to the early onset of plume formation. Progressive early onsets of plume formation predicted in figure 5.17 for 40-20 mm inlet opening sizes can be attributed to the interaction of shrinkage induced flow effect restricted to the pure melt region only. On the other hand, low cooling temperatures combined with smaller inlet opening size allows the strength of the shrinkage induced flow to grow strong enough to penetrate the mushy region itself (figure 5.18(a) and (b)). As a result, the upward movement of the solute rich melt within the mushy region adjacent to the symmetry plane of the cavity is not only hindered by the incoming shrinkage induced flow, but this naturally occurring solute rich melt is also pushed back into the mushy region leading to the redistribution of solute rich melt within the mushy region (figure 5.19(a) and (b)). The redistribution of solute rich melt within the mushy region eventually culminates to plume formation sites where the primary convection cells due to shrinkage induced flow creates a suction effect owing to the net upward movement of the melt adjacent to the mushy-liquid interface. The suppression and redistribution of the naturally occurring solute distribution within the mushy region by the stronger shrinkage induced flow results in an overall delay of the onset of plume formation. With smaller and smaller inlet opening sizes below 20 mm, the onset occurs at a more and more delayed time interval (figure 5.17). However, this fascinating effect of the inlet opening size on the onset of solutal instability is prominent only when the cavity is subjected to very low cold temperature at the bottom surface.

It is pertinent to mention here that barring few case studies involving very low intensity shrinkage induced flow associated with higher values of cold boundary temperature T_c and large inlet opening size, shrinkage induced flow always promotes early onset of solutal instability with respect to the baseline case without involving shrinkage induced flow. The early or late onset of solutal instability discussed in the present work is in the context of variation in shrinkage

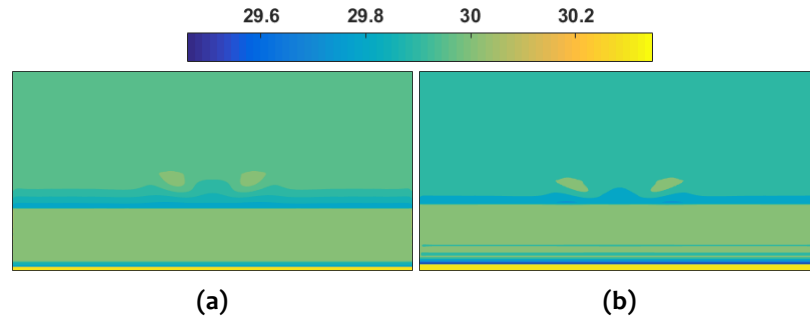


Figure 5.19 : Numerically predicted solute (Mg) distribution at the onset of solutal instability (a) $t_{onset} = 32\ s$ and $T_c = 523\ K$; (b) $t_{onset} = 19\ s$ and $T_c = 300\ K$ for $10\ mm$ inlet opening size

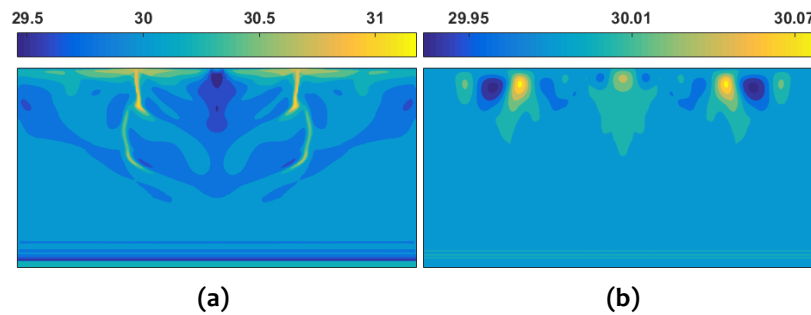


Figure 5.20 : Solute distribution after complete solidification for the case with (a) shrinkage and (b) no-shrinkage assumption for $10\ mm$ inlet opening size and $300\ K$ cold boundary temperature

induced flow intensity from lower to higher value. In fact, when the cold boundary temperature (T_c) is very low, baseline case without involving shrinkage induced flow does not even manifest channel formation. However, incorporation of the shrinkage induced flow with the same cold temperature boundary condition leads to freckle formation in solidification domain. In support of this statement, a comparison between macro-segregation pattern obtained after completion of solidification process with and without shrinkage induced flow effect is presented in figure 5.20. The case study involves solidification of Al-30 wt.% Mg alloy in the cavity with inlet opening size $10\ mm$ opening size and $T_c = 300\ K$. Shrinkage induced flow is found to assist instability to grow inside the mushy layer leading to channel formation figure. 5.20(a). However, in the absence of shrinkage induced flow, although there exist some macro-segregation profile adjacent to the top surface, it is definitely not a pattern akin to the distinctive channel formation figure. 5.20(b). Therefore, we conclude that shrinkage induced flow promotes the onset of solutal instability to grow enhancing the freckling phenomena.

5.4.7 Scaling analysis

In this subsection a scaling analysis is attempted in order to obtain a generalised understanding of the influence of shrinkage induced flow on the onset of solutal instability. The first attempt to obtain a meaningful scaling analysis involves nondimensionalization of governing equations by choosing physically relevant length-scale, time-scale, reference velocity, pressure, temperature and solute composition scales associated with the problem definition. These reference scales are reported by Worster [1992]; Heinrich et al. [2008]; Sajja and Felicelli [2011]. The reference length scale L_{ref} is considered to be of the order of primary dendrite arm spacing ($\sim 10^{-4}m$)

[Heinrich et al., 2008; Sajja and Felicelli, 2011], $u_{ref} = \sqrt{g\beta_C C_0 L_{ref}}$ [Heinrich et al., 2008], reference time-scale $t_{ref} = L_{ref}/u_{ref}$ [Heinrich et al., 2008; Sajja and Felicelli, 2011], $\rho_{ref} = \rho_l$, and $p_{ref} = \rho_l u_{ref}^2$ [Worster, 1992; Heinrich et al., 2008; Sajja and Felicelli, 2011]. Non-dimensional temperature and solute concentrations are defined as [Worster, 1992]: $\theta = (T - T_L(C_0))/(T_L(C_0) - T_e) = (T - T_L(C_0))/\Delta T$ and $\bar{C} = (C - C_0)/(C_0 - C_e) = (C - C_0)/\Delta C$. Defining other non-dimensional parameters as: $X = x/L_{ref}$, $Y = y/L_{ref}$, $\tau = t/t_{ref}$, $\bar{u} = u/u_{ref}$, $\bar{v} = v/u_{ref}$, $\bar{\rho} = \rho/\rho_{ref}$ and $\bar{p} = p/p_{ref}$ we obtain the following set of non-dimensional governing equations.

Continuity

$$\nabla \cdot (\bar{\rho} \bar{\mathbf{V}}) = \beta \frac{\partial g_l}{\partial \tau} \quad (5.9)$$

Momentum

$$\frac{\partial}{\partial \tau} (\bar{\rho} \bar{u}) + \nabla \cdot (\bar{\rho} \bar{\mathbf{V}} \bar{u}) = \frac{1}{Re} \nabla^2 (\bar{\rho} \bar{u}) - \frac{\partial \bar{p}}{\partial X} - \frac{1}{Re Da} \frac{g_s^2}{g_l^3} (\bar{\rho} \bar{u}) - \nabla \cdot \left(\frac{\rho_s g_s}{\rho_l g_l} \bar{\rho} \bar{\mathbf{V}} \bar{u} \right) \quad (5.10)$$

$$\begin{aligned} \frac{\partial}{\partial \tau} (\bar{\rho} \bar{v}) + \nabla \cdot (\bar{\rho} \bar{\mathbf{V}} \bar{v}) = \frac{1}{Re} \nabla^2 (\bar{\rho} \bar{v}) - \frac{\partial \bar{p}}{\partial Y} - \frac{1}{Re Da} \frac{g_s^2}{g_l^3} (\bar{\rho} \bar{v}) - \nabla \cdot \left(\frac{\rho_s g_s}{\rho_l g_l} \bar{\rho} \bar{\mathbf{V}} \bar{v} \right) \\ + \frac{Gr_T}{Re^2} (\theta + 1) + \frac{Gr_C}{Re^2} (\bar{C}_l + 1) \end{aligned} \quad (5.11)$$

Energy

$$\begin{aligned} \frac{\partial}{\partial \tau} (\bar{\rho} \theta) + \nabla \cdot (\bar{\rho} \bar{\mathbf{V}} \theta) = \frac{1}{Re} \left(\nabla \cdot \left(\frac{1}{Pr} \nabla \theta \right) \right) - a' \nabla \cdot (\bar{\rho} \bar{\mathbf{V}} \theta) - a' \frac{T_L(C_0)}{\Delta T} \nabla \cdot (\bar{\rho} \bar{\mathbf{V}}) \\ - \frac{\rho_s}{\rho_l} \frac{1}{Ste} \frac{\partial}{\partial \tau} (g_l) - a' \frac{\partial}{\partial \tau} (\theta g_l) - a' b' \frac{T_L(C_0)}{\Delta T} \frac{\partial}{\partial \tau} (g_l) \end{aligned} \quad (5.12)$$

where,

$$a' = \left(\frac{c_{pl}}{c_{ps}} - 1 \right); b' = 1 - \frac{\rho_s T_e}{\rho_l T_L(C_0)}$$

Species

$$\frac{\partial}{\partial \tau} (\bar{\rho} \bar{C}) + \nabla \cdot (\bar{\rho} \bar{\mathbf{V}} \bar{C}) = \frac{1}{Re Sc} \nabla \cdot (g_l \nabla \bar{C}) + \frac{1}{Re Sc} \nabla \cdot (g_l \nabla (\bar{C}_l - \bar{C})) - \nabla \cdot (\bar{\rho} \bar{\mathbf{V}} (\bar{C}_l - \bar{C})) \quad (5.13)$$

Non-dimensional parameters like contraction ratio (β), Reynolds number (Re), Darcy number (Da), thermal and solutal Grashof numbers (Gr_T and Gr_C), Prandtl number (Pr), Stefan number (Ste) and Schmidt number (Sc) appearing in Eqns. 5.9-5.13 are defined as follows:

$$\begin{aligned} \beta = \frac{\rho_s - \rho_l}{\rho_l}; Re = \frac{u_{ref} L_{ref}}{\nu}; Da = \frac{K_0}{L_{ref}^2}; \\ Gr_T = \frac{g_a \beta_T (T_L(C_0) - T_e) L_{ref}^3}{\nu^2}; Gr_C = \frac{g_a \beta_C (C_0 - C_e) L_{ref}^3}{\nu^2}; \end{aligned}$$

$$Pr = \frac{\nu}{k/(\rho_l c_{ps})}; Ste = \frac{\Delta T c_{ps}}{h_{sl}}; Sc = \frac{\nu}{D_l}$$

The nondimensional representation of conservation equations (Eqns. 5.9-5.13) has provided meaningful non-dimensional parameters like contraction ratio (β), Reynolds number (Re), Darcy number (Ds), thermal and solutal Grashof numbers (Gr_T and Gr_C), Prandtl number (Pr), Stefan number (Ste) and Schmidt number (Sc) along with many other non-dimensional groups (like a' , b' , $T_L(C_0)/\Delta T$ etc.) relevant to the alloy solidification process. However, none of these parameters helps us to characterize the onset of solutal instability with respect to the inlet opening size, cavity height, and cooling condition at the bottom boundary. In fact, the reference length scale and non-dimension scheme for temperature does not allow us to consider the effects of the cavity aspect ratio (H_C/W_C), the inlet opening size, and cooling condition at the bottom wall. While the cavity aspect ratio decides the penetration depth of the shrinkage induced flow, the ratio inlet opening size with cavity width along with cold boundary temperature (T_c) defines the magnitude of the same. Therefore, all these three aspects should be reflected in a scaling analysis to analyse the solutal instability phenomena in the presence of shrinkage induced flow, and a different approach must be considered other than the one obtained through non-dimensionalization of conservation equations (Eqns. 5.9-5.13).

The alternative scaling analysis provided here, albeit an ad-hock one in nature, is found to be much more effective in terms of predicting the dependence of solutal instability on shrinkage induced flow. In this approach, we are concerned about two different velocity scales, namely, (i) a reference velocity scale corresponding to shrinkage induced flow (u_{ref}^{sh}), and (ii) a reference velocity scale corresponding solutal buoyancy-driven flow (u_{ref}^{sb}). Estimation of u_{ref}^{sb} is similar to the one presented in the previous scaling approach, and is given by $u_{ref}^{sb} = \sqrt{g\beta_C C_0 L_{ref}}$. However, estimation of u_{ref}^{sh} is not so straight forward. To obtain u_{ref}^{sh} a semi-infinite solidification model described by Dantzig and Rappaz [2016] is used. This particular semi-infinite model defines the solid-liquid interface growth rate during the solidification of a pure substance as follows [Dantzig and Rappaz, 2016].

$$u_i^* = \phi \sqrt{\frac{\alpha_s}{t}} \quad (5.14)$$

The estimation of constant non-dimensional parameter ϕ in Eq. 5.14 involves the knowledge of phase thermal diffusivities, cold boundary temperature (T_c), initial temperature (T_i), freezing temperature (T_m), latent heat; and the transcendental equation to estimate ϕ contains all these parameters arranged in non-dimensional groups as follows [Dantzig and Rappaz, 2016].

$$\frac{\rho_s h_{sl} \alpha_s \sqrt{\pi}}{k_s (T_m - T_c)} - \frac{\exp(-\phi^2)}{\phi \operatorname{erf}(\phi)} + \sqrt{\frac{\alpha_s}{\alpha_l}} \frac{k_l}{k_s} \left(\frac{T_i - T_m}{T_m - T_c} \right) \frac{\exp(-\phi^2 \alpha_s / \alpha_l)}{\phi \operatorname{erfc}(\phi \sqrt{\alpha_s / \alpha_l})} = 0 \quad (5.15)$$

As we are dealing with alloy solidification here involving the presence of a mushy layer of finite thickness between the pure solid and liquid phases, the interface between the pure solid and mushy phase is at temperature T_e . Therefore, we replace freezing point T_m with T_e in Eq. 5.15 and estimate ϕ for given T_c and T_i . Once ϕ is calculated, considering order of magnitude for time to be unity in Eq. 5.14, we obtain a tentative scaling for growth rate of pure solid front given by; $u_i^* = \phi \sqrt{\alpha_s}$. At the very beginning of the solidification process, this semi-infinite domain consideration

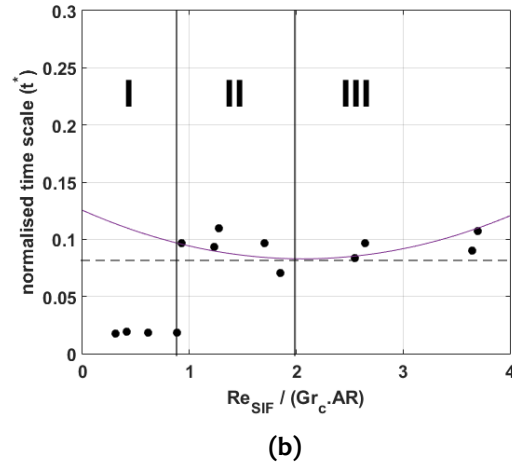
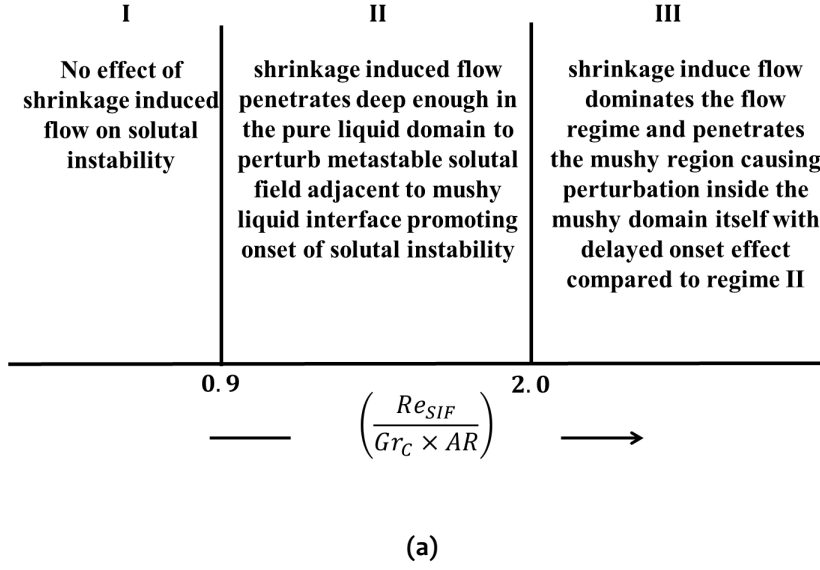


Figure 5.21 : Criterion describing the onset of solutal instability

is aptly valid. The estimation of reference scale for solid interface growth rate (u_i^*) leads to the estimation of u_{ref}^{sh} from the conservation of mass principle in the following manner.

$$\rho_l W_{in} u_{ref}^{sh} \approx (\rho_s - \rho_l) W_C u_i^* \quad (5.16)$$

Eq. 5.16 provides us with a suitable scaling for shrinkage induced flow given by $u_{ref}^{sh} = (\rho_s - \rho_l) W_C u_i^* / (\rho_l W_{in})$. The ratio of Reynolds number corresponding to incoming shrinkage flow ($Re_{SIF} = u_{ref}^{sh} L_{ref} / \nu$) and solutal Grashof number ($Gr_c = (g_a \beta_C (C_0 - C_e) L_{ref}^3) / \nu^2$) provides us with the information regarding the relative strength of these two different flow mechanisms. However, the effect of cavity aspect ratio ($AR = H_C / W_C$) still needs to be addressed. A larger value of AR indicates dissipation of shrinkage induced flow in the melt domain much above the growing mushy-liquid interface, the domain associated with the origination of solutal instability. Therefore, a higher value of AR will attenuate the effect of shrinkage induced flow on solutal instability. Combining all these physical constraints, we propose a non-dimensional group given by $Re_{SIF} / (Gr_c \cdot AR)$ in

order to classify onset behavior of solutal instability. Using this newly defined scaling parameter on case studies discussed in the previous section, we find that $Re_{SIF}/(Gr_c \cdot AR) \leq 0.9$ corresponds to no effect of shrinkage induced flow on the onset of solutal instability, *i.e.* inclusion of shrinkage induced flow does not have any effect on the onset time of the solutal instability with respect to the base line case without involving shrinkage induced flow. Condition $Re_{SIF}/(Gr_c \cdot AR) \geq 0.9$ always corresponds to the early onset of solutal instability with respect to the baseline case involving freckle formation in the absence of shrinkage. For the range $0.9 \leq Re_{SIF}/(Gr_c \cdot AR) \leq 2.0$, larger the value of $Re_{SIF}/(Gr_c \cdot AR)$ earlier is the onset of solutal instability figure 5.21 (a)-(b). However, for $Re_{SIF}/(Gr_c \cdot AR) > 2.0$ this trend is reversed, *i.e.*, larger the value of $Re_{SIF}/(Gr_c \cdot AR)$ more delayed is the onset of solutal instability figure 5.21 (a)-(b).

5.5 SUMMARY

Effect of grid resolution and time-step resolution on the simulation results are carried out for solidification process involving freckle formation in the presence of shrinkage induced flow. Al-30 wt.% Mg is considered to the model binary system. It is inferred that the phenomena is highly unstable, and achieving complete grid resolution and time-step independence is not possible. Model validation is performed with respect to a benchmark problem involving inverse segregation obtained for the bottom-up solidification of Al-4.1 wt.% Cu alloy in the presence of shrinkage induced flow and characterized by heavier solute rejection in the melt during liquid-solid phase transition. Simulation result from the proposed model is compared with existing numerical and experimental data reported in literature, furnishing reasonably good agreement. General attributes of shrinkage induced flow on freckle formation is studied for a very high value of cold boundary temperature ($T_c = 720K$) while keeping inlet opening size to be 40 mm. The results inferred that the convection field in the melt region at the initial stage of the solidification process is governed solely by the shrinkage induced flow, followed by the advent of the solutal instability adjacent to mushy liquid interface leading to complex flow interactions. One of the major influence of the shrinkage induced flow is manifested by the lateral bending of plumes away from the central plane of symmetry leading to the formation of oblique channels. Case study involving the effect of varying inlet opening size is analysed for $T_c = 700K$. It is inferred from the study that the opening size has a substantial impact on the severity of the solute lean region near the opening. The severity of negative segregation adjacent to the opening at the cavity top surface varies from severe to mild entrapment of solute lean composition for small to full opening. Next, the effect of cold temperature on the onset of instability and macro-segregation is investigated. A shift of cooling temperature at the bottom surface from high to moderately low range causes the onset of the solutal instability to occur at a comparatively greater height of the mushy-liquid interface. However, further reduction of bottom surface temperature intensifies the strength of shrinkage induced flow, allowing it to perturb the meta-stable solutal field adjacent to the mushy-liquid interface at an early stage of solidification, leading to an early onset of solutal instability. Low cooling temperature also negates the severity of the negative segregation. However, for the entire range of cooling, the thickness of the mushy layer is always found to be greater in the presence of shrinkage induced flow as compared to the predicted mushy layer thickness obtained under the no-shrinkage assumption. The thicker mushy region obtained under the influence of shrinkage induced flow is attributed to the entrainment of fresh melt with nominal composition into the upper bound of the mushy layer, leading to an overall elevation of local liquidus temperature in that region. In order to investigate the effect of cooling on the onset of solutal instability, a case study is carried out by varying the cold boundary temperature while considering the central opening sized at the upper surface of the cavity to be 40 mm. In terms of onset timing, the results involving shrinkage induced flow consistently predicted early onset of solutal instability as compared to those obtained with no shrinkage assumption. With low cooling temperatures, the onset time difference became substantially large between the studies associated with shrinkage

and no-shrinkage assumptions. In terms of the height of the mushy-liquid interface, for high and moderate cold temperatures, solutal instability is found to be triggered at a lower position of this interface in the absence of shrinkage induced flow. However, the gap between the onset locations with and without shrinkage induced flow assumptions in terms of mushy-liquid interface heights diminishes as the cold boundary temperature is lowered, leading to a cross over point below a certain range of T_c . Further lowering of the cold boundary temperature consistently reduces the mushy-liquid interface height corresponding to the onset of solutal instability for shrinkage induced flow assumption, which is completely contrary to the ever-increasing behavior of the same under the no-shrinkage assumption. Effect of shrinkage induced flow on the onset of solutal instability being more prominent for large cooling, the influence of cavity inlet opening size is revisited considering T_c at 523 K while varying the opening size from 40-6 mm. Over the range of opening size 40-20 mm, both time interval and mushy-liquid interface height corresponding to the onset of solutal instability manifested a monotonically decreasing trend signifying the early onset of solutal instability. The early onset of plume formation for this range of inlet opening size (40-20 mm) is attributed to the perturbation of the meta-stable solutal buoyancy field by the shrinkage induced flow within the pure melt region only. However, lowering the opening size below 20 mm intensifies the shrinkage induced flow significantly and allows it to penetrate the mushy region itself, leading to the suppression and redistribution of naturally occurring solutal instability of the liquid phase within the mushy layer. The redistribution of the solute rich melt inside the mushy layer eventually leads to plume formation sites along the path of least resistance where primary circulations corresponding to shrinkage induced flow lifts off the fluid from the mushy-liquid interface to the pure melt domain. The entire process of suppression and redistribution of the solutal instability within the mushy region leads to an overall delay of the onset of plume formation, and this effect is evident only when the solidification process is simultaneously subjected to large cooling and small inlet opening size. A scaling analysis is attempted to have a criterion that assesses the relative magnitude of shrinkage convection and solutal buoyancy-driven natural convection. A non-dimensional group in the form $Re_{SIF}/(Gr_c \cdot AR)$ is proposed. It was inferred that $Re_{SIF}/(Gr_c \cdot AR) \leq 0.9$ corresponds to no effect of shrinkage induce flow on the onset of solutal instability. Condition $Re_{SIF}/(Gr_c \cdot AR) \geq 0.9$ always corresponds to the early onset of solutal instability with respect to the baseline case involving freckle formation in the absence of shrinkage. For the range $0.9 \leq Re_{SIF}/(Gr_c \cdot AR) \leq 2.0$, larger the value of $Re_{SIF}/(Gr_c \cdot AR)$ earlier the onset of solutal instability. However, for $Re_{SIF}/(Gr_c \cdot AR) > 2.0$ this trend is reversed, i.e. larger the value of $Re_{SIF}/(Gr_c \cdot AR)$ later the onset of solutal instability.

...